~~CONFIDENTIAL~~

Copy 34
RM E50D10

~~53-29-50~~

E 50 D10

NACA RM E50D10

NACA

RESEARCH MEMORANDUM

AERODYNAMIC CHARACTERISTICS OF NACA RM-10 MISSILE IN 8- BY 6-FOOT SUPERSONIC WIND TUNNEL AT MACH NUMBERS FROM 1.49 TO 1.98

I - PRESENTATION AND ANALYSIS OF PRESSURE MEASUREMENTS (STABILIZING FINS REMOVED)

By Roger W. Luidens and Paul C. Simon

Lewis Flight Propulsion Laboratory
Cleveland, Ohio

6598

[redacted] DOCUMENT

~~This document contains classified information affecting the National Defense of the United States within the meaning of the Espionage Act, USC 50:31 and 32. Its transmission or the revelation of its contents in any manner to an unauthorized person is prohibited by law. Information so classified may be imparted only to persons in the military and naval services of the United States, appropriate civilian officers and employees of the Federal Government who have a legitimate interest therein, and to United States citizens of known loyalty and discretion who of necessity must be informed thereof.~~

RECEIVED
28 JUL 1950
HOLLOMAN
AFB N. M.

NATIONAL ADVISORY COMMITTEE FOR AERONAUTICS
WASHINGTON
July 20, 1950

~~CONFIDENTIAL~~

319.98/13

~~57-578~~

NATIONAL ADVISORY COMMITTEE FOR AERONAUTICS

RESEARCH MEMORANDUM

AERODYNAMIC CHARACTERISTICS OF NACA RM-10 MISSILE IN 8- BY 6-FOOT SUPERSONIC WIND TUNNEL AT MACH NUMBERS FROM 1.49 TO 1.98

I - PRESENTATION AND ANALYSIS OF PRESSURE MEASUREMENTS

(STABILIZING FINS REMOVED)

By Roger W. Luidens and Paul C. Simon

SUMMARY

An experimental investigation of the pressure distribution on a slender pointed body of revolution was conducted in the NACA Lewis 8- by 6-foot supersonic wind tunnel at free-stream Mach numbers of 1.49, 1.59, 1.78, and 1.98, and at a Reynolds number based on model length of approximately 30,000,000 over a range of angles of attack. The body was a half-scale model of the fuselage of the NACA supersonic flight research missile designated RM-10 (with the stabilizing fins removed). The pressure distribution over the entire length of the body at zero angle of attack agreed well with that predicted by linearized theory. At angle of attack, the experimental pressure distributions showed close agreement with an improved linearized theory at all points on the model surface except over the aft leeward portion of the body, where the pressure distribution was appreciably modified as a result of viscosity effects. A survey of the stream total pressure in the plane of the model base indicates that at angle of attack the boundary-layer air formed a pair of lobes located on the leeward side of the body, which left a very thin boundary layer on the windward side. At zero angle of attack, the boundary-layer profile and thickness agreed very well with the values calculated for subsonic turbulent flow for a flat plate. Base-pressure measurements are also presented.

INTRODUCTION

Several methods are available for theoretically estimating the pressure distribution, and forces and moments on a slender pointed body of revolution. Experimental evaluations of these methods, however, have been limited primarily to the study of projectiles, usually at low Reynolds numbers. An investigation has therefore been conducted

[redacted]

in the NACA Lewis 8- by 6-foot supersonic wind tunnel to determine the aerodynamic load distributions on the NACA supersonic research missile RM-10. The pressure distribution over the body has been determined by experimental means and a comparison has been made with the predicted distribution calculated by an improved linearized theory. Where deviations of the experimental results from the theory are observed, a rational explanation is given on the basis of shed vorticity and viscosity effects. In order to further evaluate these effects, a survey of the pitot pressures in the plane of the model base has been made.

The investigation was conducted at free-stream Mach numbers of 1.49, 1.59, 1.78, and 1.98 for a range of angles of attack from 0° to 9°, and at a Reynolds number of approximately 30,000,000.

SYMBOLS

The following symbols are used in this report:

a	local velocity of sound
C_p	pressure coefficient, $(p-p_0)/q_0$
c	constant
l	length of model
M	Mach number
P	total pressure
p	static pressure
q	$\frac{\gamma}{2} pM^2$
Re	Reynolds number, $\rho U l/\mu$
U_0	free-stream velocity
U_L	local stream velocity outside boundary layer
u	velocity in boundary layer
v_r	radial velocity component (cylindrical coordinates)

1296

v_x	axial velocity component
v_θ	tangential velocity component (cylindrical coordinates)
x,b	coordinates of model
x,r,θ	cylindrical coordinates ($\theta = 0$ in plane of angle of attack and to windward)
y	distance perpendicular to and with origin at model surface
α	angle of attack
β	cotangent of Mach angle, $\sqrt{M^2-1}$
γ	ratio of specific heats, 1.40
δ	boundary-layer thickness
μ	viscosity
ρ	density
φ	velocity potential

Subscripts:

b	base of model
h	sting
m	measured behind normal shock at local stream Mach number
0	free-stream conditions
1	conditions for model at zero angle of attack
2	conditions for model due to angle of attack

APPARATUS AND PROCEDURE

The investigation was conducted in the NACA Lewis 8- by 6-foot supersonic wind tunnel. This nonreturn-type tunnel is powered by three 29,000-horsepower electrical motors that drive a 7-stage axial-flow compressor located upstream of the test section. Air is filtered and dried before entering the compressor. The supersonic nozzle is formed by two adjustable steel-plate walls that are actuated by a series of hydraulic jacks to give a nominal Mach number range of 1.4 to 2.0. The Reynolds numbers corresponding to the test Mach numbers are shown in the following table:

Free-stream Mach number, M_0	Reynolds number, Re (based on model length)
1.49	28,000,000
1.59	29,000,000
1.78	31,000,000
1.98	28,000,000

Condensation-free flow was maintained during each run.

The model (fig. 1) consisted of the half-scale RM-10 fuselage (stabilizing fins removed), which is a body of revolution with a parabolic profile defined by the equation

$$b = \sqrt{\frac{c}{2}}\,x\left(2 - \frac{x}{45}\right)$$

$$0 \leq x \leq 73.25 \qquad (1)$$

where

$$c = \frac{2}{15^2}$$

A machined straight taper existed between stations 66 and 71.5. (Station numbers represent distance from station 0 in inches.) The body was spun from aluminum sheet and the nose was blunted by removing 1/4 inch from the tip. The model has an over-all length of 73 inches, a maximum diameter of 6 inches, and a fineness ratio of 12.2.

The deviation of the model from the parabolic contour is shown in figure 2(a). Relatively large deviations occur in the vicinity of station 20. This discrepancy is also apparent in the curvature (fig. 2(b)), which was measured by a gage with a spacing of 1.5 inches between its three contact points. (A joint existed at station 24.2 and a small eccentricity resulting in an asymmetrical discontinuity in the model contour was observed at this juncture after most of the runs.) Because of model irregularities, some scatter in the experimental pressure-distribution data is to be expected.

The static-pressure orifices on the model surface were arranged in two diametrically opposite rows and were located at the longitudinal stations given in figure 1. At station $73\frac{1}{4}$, base-pressure tubes were located at ±45° to each of the rows of surface statics and at a radius of 1.62 inches. Two boundary-layer rakes extending $1\frac{3}{4}$ inches into the stream were located in the plane of the surface static-pressure orifices. The model could be rotated about its longitudinal axis by an internal mechanism with a travel in excess of 90°, so that assuming flow symmetry, the pressures at any rotational position on the model could be obtained. During the investigation, pressures were recorded at rotational positions of the model of $\theta = 0^\circ$, 10°, 30°, 50°, 70°, 90°, 110°, 130°, 150°, 170°, and 180°.

The model was supported from its base by a sting extending upstream from the tunnel vertical strut (fig. 3). The sting was designed by the criteria of reference 1 for attaining minimum interference with the model base pressure at zero angle of attack. Angle of attack was obtained by movement of the tunnel vertical strut. The center of rotation of the system was located forward of the maximum section of the model.

Actual angles of attack were determined by an electrical oil-damped pendulum-type indicator located in the forward section of the model. The actual angles of attack are compared with the nominal angle of attack for each Mach number investigated in the following table:

Angle of attack, deg		
Nominal	Actual	
	Mach number, M_0	
	1.59	1.49, 1.78, 1.98
0	0	0
2	1.9	1.8
4	4.2	4.0
6	5.9	5.8
9	8.9	8.6

The theoretical curves were calculated for the actual angle of attack in each case. Static pressures on the model and the sting, as well as the pitot pressures of the boundary-layer survey rake, were obtained on manometer boards using tetrabromoethylene and mercury, respectively, as fluids. All pressures were photographically recorded.

REDUCTION OF DATA

In the calculation of the pressure coefficient, the free-stream static pressure was determined as the average pressure measured by several tunnel-wall static orifices located opposite the nose of the model. The free-stream Mach number was determined from the ratio of the free-stream static pressure in the test section and the average of total pressures measured in the subsonic flow upstream of the tunnel throat. This Mach number checked well with the Mach number determined by tunnel calibration. The ratio of specific heats γ was taken as 1.40.

The increments of pressure coefficient due to angle of attack were determined by subtracting the measured value at zero angle of attack from measured values at angle of attack.

In order to determine boundary-layer velocity profiles, the Rankine-Hugoniot equations were used to evaluate the rake data by assuming that the static pressure in the flow field is constant along radial lines and equal to the value measured at the model surface, and that the total temperature in the flow field is constant.

THEORY

Pressure distributions. - The linearized theory was used to estimate the velocity field around the body. Velocity components associated with thickness and angle of attack were independently calculated and superimposed on the free-stream velocity components. The pressure distribution was then evaluated from the resultant velocity field.

Perturbation velocity components on the body surface at zero angle of attack may be evaluated by the methods of references 2 or 3.

$$\left.\begin{aligned}
&\frac{\partial\varphi_1}{\partial x} \quad \text{(See equation (12)}\\[2ex]
&\frac{\partial\varphi_1}{\partial r} = U_0 \frac{db}{dx}\\[2ex]
&\frac{1}{r}\frac{\partial\varphi_1}{\partial\theta} = 0
\end{aligned}\right\} \qquad (2)$$

In terms of axes fixed with respect to the body, the velocity components associated with angle of attack are from reference 4: (The approximations $\sin\alpha = \alpha$ and $\cos\alpha = 1$ have been made in the equations for the perturbation velocities.)

$$\left.\begin{aligned}
&\frac{\partial\varphi_2}{\partial x} = -2U_0\alpha \cos\theta \frac{db}{dx}\\[2ex]
&\frac{\partial\varphi_2}{\partial r} = U_0\alpha \cos\theta\\[2ex]
&\frac{\partial\varphi_2}{r\partial\theta} = U_0\alpha \sin\theta
\end{aligned}\right\} \qquad (3)$$

The free-stream velocity components in terms of coordinates fixed in the body are

$$\left.\begin{aligned}
&\frac{\partial\varphi_0}{\partial x} = U_0 \cos\alpha\\[2ex]
&\frac{\partial\varphi_0}{\partial r} = -U_0\alpha \cos\theta\\[2ex]
&\frac{\partial\varphi_0}{r\partial\theta} = U_0\alpha \sin\theta
\end{aligned}\right\} \qquad (4)$$

(The approximation $\cos \alpha = 1$ is not permissible in the first equation of equation (4) because $U_0 \cos \alpha$ is of lower order than a perturbation velocity. Such an approximation would lead to an error in $\partial\varphi_0/\partial x$ of the order of magnitude of a perturbation velocity.)

Addition of the respective velocity components from equations (2), (3), and (4) gives for the body surface

$$\left.\begin{aligned} v_x &= U_0 \cos \alpha + \frac{\partial\varphi_1}{\partial x} - 2U_0\alpha \cos \theta \frac{db}{dx} \\ v_r &= U_0 \frac{db}{dx} \\ v_\theta &= 2U_0\alpha \sin \theta \end{aligned}\right\} \qquad (5)$$

From an expansion of the exact expression for the pressure coefficient, an approximate expression results:

$$C_p = \frac{U_0{}^2 - (v_x{}^2+v_r{}^2+v_\theta{}^2)}{U_0{}^2} \qquad (6)$$

Substitution of equation (5) into equation (6) and dropping all terms of higher order than α^2 $\left(\text{or } \alpha \frac{db}{dx}, \text{ and so forth}\right)$ gives

$$C_p = - \frac{2}{U_0} \frac{\partial\varphi_1}{\partial x} - \left(\frac{db}{dx}\right)^2 + 4\alpha \cos \theta \frac{db}{dx} + \alpha^2(1-4 \sin^2 \theta) \qquad (7)$$

The pressure coefficients associated with thickness and angle of attack are additive and are separately given as

$$C_{p,1} = - \frac{2}{U_0} \frac{\partial\varphi_1}{\partial x} - \left(\frac{db}{dx}\right)^2 \qquad (8)$$

$$C_{p,2} = 4\alpha \cos \theta \frac{db}{dx} + \alpha^2(1-4 \sin^2 \theta) \qquad (9)$$

An alternate and independent derivation of this result is presented in reference 5. Equations (8) and (9) have been frequently approximated, respectively, by

$$C_{p,1} = -\frac{2}{U_0}\frac{\partial\varphi_1}{\partial x} \tag{10}$$

$$C_{p,2} = 4\alpha \cos\theta \frac{db}{dx} \tag{11}$$

For the particular body discussed herein, defined by equation (1), the method of reference 2 gives

$$\frac{\partial\varphi_1}{\partial x} = -U_0 c \left\{ \frac{3-9\left(\frac{x}{45}-1\right)}{2}\sqrt{\left(\frac{x}{45}\right)^2 - \beta^2\left(\frac{b}{45}\right)^2} + \left[3\left(\frac{x}{45}-1\right)^2 - 1 + \frac{3}{2}\beta^2\left(\frac{b}{45}\right)^2\right]\cosh^{-1}\frac{x}{\beta b} \right\} \tag{12}$$

Also

$$\frac{db}{dx} = -2\sqrt{\frac{c}{2}}\left(\frac{x}{45}-1\right) \tag{13}$$

Substitution of equations (12) and (13) into equations (7), (8), and (9) gives the theoretical pressure distribution of the RM-10.

Boundary layer. - For a simple correlation of the measured boundary layer with theory, several curves are presented from reference 6, which derives from the data for turbulent subsonic flow through pipes the relation

$$\frac{u}{U_L} = \left(\frac{y}{\delta}\right)^{1/7} \tag{14}$$

for the nondimensional velocity ratio profile in terms of the nondimensional distance ratio from the friction surface. The equation for the boundary-layer thickness on a flat plate corresponding to the velocity profile of equation (14) is

$$\delta = 0.37\, l \left(\frac{\mu_0}{\rho_0 U_0 l} \right)^{1/5} \tag{15}$$

Equation (15) is applied to evaluate the theoretical boundary-layer growth on the RM-10.

RESULTS AND DISCUSSION

The experimental results consist of pressure distributions on the body surface, including base-pressure measurements, and a boundary-layer (pitot pressure) survey in the plane of the model base. These results are discussed for zero angle of attack and for angle of attack.

Zero Angle of Attack

Pressure distribution. - The experimental variation of the pressure coefficient with longitudinal position on the body at zero angle of attack is presented in figure 4 for all Mach numbers investigated. Compared with the experimental data are the theoretical curves computed from the linearized theory (equations (8) and (10)) for the parabolic contour of equation (1). To account for the machined straight taper from stations 66 to $71\frac{1}{2}$, the step-by-step integration method of reference 3 was also used to calculate the theoretical pressures of figure 4(c).

The trends for the theoretical and experimental curves were similar and the agreement was best with the refined calculation of equation (8). The pressure coefficients were high near the nose of the model, then decreased rapidly to negative values near and downstream of the body maximum section. Much of the data-point scatter may be explained on the basis of local model variations from the assumed contour. The effect of changes in model contour is illustrated by the jog in the theoretical pressure-distribution curve (fig. 4(c)), which includes the effect of the machined straight taper. The data at Mach number of 1.49 show evidence of a pressure gradient in the free-stream flow for this particular run.

Base pressures. - Base and sting pressures are included in figure 4. The pressure on the sting 1/4-inch downstream of the base was the same as the base pressure, both being below free-stream static pressure. At 3 inches downstream of the model base, the sting pressure recovered to a value above free-stream static pressure.

The variation of base-pressure coefficients for zero angle of attack for the Mach numbers investigated is shown in figure 5. The boundary-layer rakes were removed for this measurement to avoid interference effects. Included for comparative purposes are data from references 1, 7, and 8. The data from reference 1 show the effect of boattailing and of laminar and turbulent boundary layers at Mach number 1.5. The result from this investigation shows only a tendency to agree with the base-pressure coefficient for the body with boattailing and with turbulent boundary layer, the condition most similar to conditions of this investigation. The variation of base pressure with Mach number was small, a trend that compares fairly well with the data of references 7 and 8.

Boundary layer. - The pitot pressures in the plane of the model base are reduced as boundary-layer data and are presented in figure 6 in terms of nondimensional velocity and distance ratio. Also included is the theoretical 1/7-power-law profile of equation (14). The correlation of the data with the 1/7-power profile shows that the boundary layer is turbulent. The velocity-ratio profile is independent of Mach number in the range of the investigation. Included with the plot is a table giving the sonic value of the nondimensional velocity. The sonic point is within 1/8 of the boundary-layer thickness from the model surface.

A comparison of the observed boundary-layer thickness with the thickness predicted by equation (15) for subsonic turbulent boundary layer on a flat plate is presented in figure 7. The boundary-layer thickness is fairly well predicted over the range of Mach numbers. Boundary-layer data were influenced by pressure gradients, three-dimensional effects, and density variations, and therefore only qualitative agreement should be expected with the formulations for the subsonic turbulent boundary layer on a flat plate.

Angle of Attack

Pressure distribution. - The longitudinal pressure distributions along the top, bottom, and sides of the model for angles of attack of 4° and 9° and for the Mach numbers investigated are presented in figure 8. The incremental changes in pressure coefficient with angle of attack determined from figures 4 and 8 are plotted in figure 9. According to equation (9), these incremental changes are independent of Mach number.

In accordance with the theory for a parabolic contour, the experimental variation of the pressure coefficient due to angle of attack on the windward side of the model (fig. 9(a)) with the longitudinal distance was approximately linear. Increases in angle of attack were accompanied by increases in the pressure near the nose and increases in the rate of pressure drop with longitudinal position. These data, in general, substantiate the theory for predicting the pressure due to angle of attack both as to independence of Mach number and magnitude of the pressure over the entire length of the model. The experimental values, however, tend to fall slightly above the theoretical curves.

On the leeward side of the model (fig. 9(b)), the observed effect of angle of attack was to decrease the pressures on the forward portion of the model in the manner predicted by theory. Angle of attack had little effect on the pressures over the downstream portion of the body (implying flow separation), although the theory indicates that a considerable increase in pressure should exist. Despite the deviations of the data from the theory in magnitude, an independence of Mach number remained evident over most of the model length.

The increment of pressure due to angle of attack on the side of the model (fig. 9(c)) is predicted by theory to be independent of the body profile or station as well as independent of Mach number, and the effect of angle of attack is to decrease the pressure on the side of the model proportional to the square of the angle of attack. The experimental data show good agreement with the theory over most of the model length. At the rear of the model the experimentally determined increment of pressure coefficient tends to zero; however, an independence of Mach number remains evident. A similar effect was observed on the leeward side of the model.

The experimentally observed pressure distributions as a function of the angular coordinate around the body are presented in figures 10 to 13 for several representative stations and for the Mach numbers and angles of attack investigated. From these data the incremental pressure coefficients due to angle of attack were obtained and plotted in figure 14. Over the forward portion of the model (figs. 14(a) to 14(c)), the pressures at the bottom and top of the model increased and decreased, respectively, and there was a marked reduction in pressure at the side of the model. The agreement with the theory (equation (9)) is good both as to the independence of Mach number and the predicted value of the pressure coefficient. (The pressure due to angle of attack predicted by equation (11) illustrated in figure 14(a) deviates considerably from the experimental pressure distribution around the model.)

1296

Over the rear portion of the model (figs. 14(d) to 14(f)), the experimental pressure distribution curves continue to show a reduction in pressure near the sides of the model. The pressures on the windward side of the model agreed well with those predicted by theory; whereas on the leeward side of the model, deviations between experimental and theoretical pressures progressively increased in magnitude and extent as the station increased.

Deviations of the incremental pressure from the values predicted by theory to values approximately equal to zero, such as occurred over the aft leeward portion of the model, might be interpreted as an indication of flow separation; flow separation in the conventional sense did not occur, however, as shown by the pitot-pressure measurements at the model base.

Pitot-pressure contours. - Contours of the ratio of static pressure to free-stream total pressure p/P_0 at station 70 and of the ratio of pitot pressure to free-stream total pressure P_m/P_0 in the plane of the base of the model are shown in figures 15 and 16. (At the large angles of attack, the measured pitot pressures may be somewhat in error because of angularity between the stream direction and axes of the pitot tubes.)

At zero angle of attack (fig. 15(a)), the contours of pitot pressure and static pressure on the model surface are symmetrical around the body, as would be expected. At an angle of attack of 2° (fig. 15(b)) the contours in general became crowded on the windward side of the model and separated on the leeward side. At the same time the static pressure on the model surface varied in the direction predicted in the theory, becoming less than the pressure at zero angle of attack on the windward side of the model $(\theta = 0^{\circ})$ and greater on the leeward side.

At increased angles of attack of 4° and 6° (figs. 15(c) and 15(d)), the contours continued to approach the model surface on the windward side of the model, while on the leeward side of the model the pitot contours formed a lobe in the vicinity of $\theta = 150^{\circ}$. (The individuality in the movement of the $P_m/P_0 = 0.8$ contour on the windward side of the model with angle of attack is associated with the potential flow field about the body.) The variation in static pressure on the windward side of the model followed expected behavior by further decreasing in value from $(p/P_0)_1$; however, on the leeward side of the model a trend reverse of that predicted by theory and counter to that observed at an angle of attack of 2° occurred, in that the static pressure decreased with an increase in angle of attack from 2° to 6°. At 9° angle of attack (fig. 15(e)), the static pressure on the windward side of the model generally followed the previously indicated trends. On the leeward side of the model the trends observed at angles of attack of 4° and 6° are accentuated; the lobe increases in size and the static pressure on the model surface continues to decrease. The pitot contours for Mach numbers of 1.49, 1.59, and 1.98 are similar in character to those presented for Mach number 1.78. The pitot contours at an angle of attack of 6° for the remaining Mach numbers in figure 16 are representative.

With certain assumptions, the boundary-layer distribution about the model base at angle of attack may be calculated. The measured pitot pressure results from either one or a combination of (1) the effect of viscous losses and (2) the effect of shock losses. The shock losses are affected by the local Mach number, which will deviate from that predicted by potential flow theory due to the presence of viscous losses and vorticity effects. Insufficient test information is available to make possible the experimental separation of the aforementioned effects. The assumption that the static pressure in the flow field is constant along radial lines at the value measured at the model surface, however, permits reduction of the data as boundary-layer velocity ratios which are of interest. Because the validity of the assumption becomes more doubtful as the angle of attack increases, especially in the regions where vorticity may be expected to exist, only the pitot-pressure distribution at angles of attack of 0° and 4° and Mach number 1.78 (represented in figs. 15(a) and 15(c)) are presented in figure 17 as contours of u/U_L. As a result of the angle of attack, a pronounced thickening of the boundary layer in the vicinity of $\theta = 150^\circ$ and a thinning of the boundary layer on the windward side of the model are evident on this plot. In general, it is believed that the pitot contours can be interpreted to give a fair qualitative picture of the boundary-layer distribution about the base of the model for the angles of attack investigated.

The schlieren photographs (fig. 18) of the forward part of the model for $\alpha = 6^\circ$ and $M = 1.78$ indicate a greater thickness of boundary layer on the leeward side of the model. Consequently, it may be assumed that the boundary layer thickens on the leeward side of the model for all stations along the model.

As indicated by the pitot contours, the pitot tube nearest the model surface $(y = 1/16$ inch) recorded a pressure greater than the local surface static pressure for all circumferential positions around the model. Consequently, it can be concluded that flow separation has not occurred, in the sense that both the velocity and velocity gradient have not become zero within 1/16 inch of the model surface. The shape of the pitot contours, however, indicates that the mechanisms at work within the flow warrant further discussion.

Flow mechanism. - As an aid to understanding the significance of the data presented, a discussion is given of the flow mechanism that may be deduced from the data of this investigation. In order to follow the aft leeward portion of the body, the flow must traverse increasingly adverse pressure gradients as it proceeds downstream. (See theoretical curves $C_{p,1}$ and $C_{p,2}$, figs. 4 and 14.) The influence of viscosity also increases as the flow proceeds downstream. As a consequence of these two factors, a "separation of the cross flow" occurs that mitigates the pressure gradient the flow is required to traverse. (That is, although the static pressures are characteristic of separation, the axial component of the flow has not separated as has been shown by the pitot pressures. The point of cross-flow separation is characterized by the cross-flow velocity and velocity gradient becoming zero at the body surface.) The lowering of the static pressures to values less than theoretical over the top side of the model contributes an additional lift to the model; consequently, a simultaneous formation of vorticity must also have occurred. The existence of the vorticity may also be implied from the pair of lobes (rather than a single hump) formed on the pitot contours. (Reference 9 makes use of the concept of the separation of the cross flow around a slender body of revolution inclined to a stream to calculate lift, drag, and moment. The mechanisms of the flow for the present supersonic case are similar to the subsonic case of an elongated body of revolution at angle of attack (reference 10).)

Further evidences of the hypothesis of the cross-flow separation due to viscous effects and the simultaneous formation of vorticity may be deduced from the qualtitative similarity both in extent and shape of the total-pressure-ratio profiles at angle of attack with photographs of the two-dimensional subsonic flow about a cylinder showing the vortices in the wake of the cylinder. (For example, the photographs of reference 11.) In the subsonic case this phenomenon is known to be a result of viscosity and is associated with vorticity. Recent experimental and theoretical investigations at the NACA Ames laboratory have shown that the cross flow around an inclined body of revolution in a supersonic stream is qualitatively similar to the flow normal to a circular cylinder which has been set in motion from rest and has traveled insufficient time for the development of steady state flow. Flow-visualization studies have also established that the flow field about a body at moderate angle of attack contains two symmetrically disposed vortices on the lee side of the body. The cores of these vortices are alined approximately with the free stream.

The location of the vorticity along the length of the model may be traced by examining the series of surface static-pressure distributions around the body shown in figures 10 to 14. Because the angles of attack investigated were moderate, the vorticity remains near the body surface and the low static pressure of the vortex core influences the body static pressures. The low local static pressure at an angular position θ of approximately 150° corresponds to the location of vortex cores and agrees with the location indicated by the pitot contours at the base of the model.

Base pressures. - The variation with angle of attack of base-pressure coefficient due to angle of attack for the Mach numbers investigated is shown in figure 19. (The angle of attack for each run proceeded from 0° to 9°.) The boundary-layer rakes were removed for this investigation; however, the reliability of these data must still be considered in light of the sting system supporting the model. The observed effect of angle of attack is to decrease the base pressure, although this effect is small for small angles (4°). For the purpose of comparing the magnitude of the effect of angle of attack with the effect that occurs on the remainder of the model, and as a point of general interest, equation (9), evaluated at $\theta = 90^\circ$, is presented with the data. (At $\theta = 90^\circ$ the increment of pressure due to angle of attack is independent of body profile.) There is no theoretical reason to expect agreement between the data and the equation.

SUMMARY OF RESULTS

The pressure distribution over a slender-pointed body of revolution was investigated in the NACA Lewis 8- by 6-foot supersonic wind tunnel at free-stream Mach numbers of 1.49, 1.59, 1.78, and 1.98 at a Reynolds number of approximately 30,000,000 over a range of angles of attack. The following results were obtained:

1. The pressure distributions at zero angle of attack agreed closely with those predicted by linearized theory.

2. The boundary-layer profiles measured at the aft end of the body for 0° angle of attack showed close agreement with the 1/7-power law for subsonic flow. The boundary-layer thickness showed reasonable agreement with the values predicted by the subsonic equation, corresponding to the 1/7-power law for predicting the thickness on a flat plate.

3. The experimental pressure distribution due to angle of attack showed close agreement with the independence of Mach number predicted by linearized theory and with magnitude of the pressure predicted for the forward portion of the body, and for the entire length of the windward portions of the body. The pressure distributions on the aft-leeward portion of the body indicated that viscosity and vorticity are of major importance in this region.

4. The measured pitot pressures on the plane of the model base and schlieren photographs showed a pronounced shift of the boundary layer from the windward to the leeward side of the body at angle of attack.

5. The base-pressure coefficient was essentially independent of Mach number between 1.6 and 2.0 for angles of attack from 0° to 4°. Increasing the angle of attack reduced the base pressure.

Lewis Flight Propulsion Laboratory,
National Advisory Committee for Aeronautics,
Cleveland, Ohio.

REFERENCES

1. Perkins, Edward W.: Experimental Investigation of the Effects of Support Interference on the Drag of Bodies of Revolution at a Mach Number of 1.5. NACA RM A8B05, 1948.

2. Jones, Robert T., and Margolis, Kenneth: Flow over a Slender Body of Revolution at Supersonic Velocities. NACA TN 1081, 1945.

3. von Kármán, Theodor, and Moore, Norton B.: Resistance of Slender Bodies Moving with Supersonic Velocities, with Special Reference to Projectiles. Trans. A.S.M.E., vol. 54, no. 23, Dec. 15, 1932, pp. 303-310.

4. Tsien, Hsue-Shen: Supersonic Flow over an Inclined Body of Revolution. Jour. Aero. Sci., vol. 5, no. 12, Oct. 1938, pp. 480-483.

5. Allen, H. Julian: Pressure Distribution and Some Effects of Viscosity on Slender Inclined Bodies of Revolution. NACA TN 2044, 1950.

6. von Kármán, Th.: On Laminar and Turbulent Friction. NACA TM 1092, 1946.

7. Kurzweg, H. H.: The Pressure at the Base of Bodies at Supersonic Speeds. Memo. 9609, Naval Ord. Lab., March 31, 1948. (Proj. No. NOL-Re9d-21-2.)

8. Katz, Ellis: Flight Investigation from High Subsonic to Supersonic Speeds to Determine the Zero-Lift Drag of a Transonic Research Vehicle Having Wings of 45° Sweepback, Aspect Ratio 4, Taper Ratio 0.6, and NACA 65A006 Airfoil Sections. NACA RM L9H30, 1949.

9. Allen, H. Julian: Estimation of the Forces and Moments Acting on Inclined Bodies of Revolution of High Fineness Ratio. NACA RM A9I26, 1949.

10. Harrington, R. P.: An Attack on the Origin of Lift of an Elongated Body. Pub. No. 2, Daniel Guggenheim Airship Inst., 1935, pp. 32-52.

11. Prandtl, L., and Tietjens, O. G.: Applied Hydro- and Aeromechanics. McGraw-Hill Book Co., 1934, pp. 6-13.

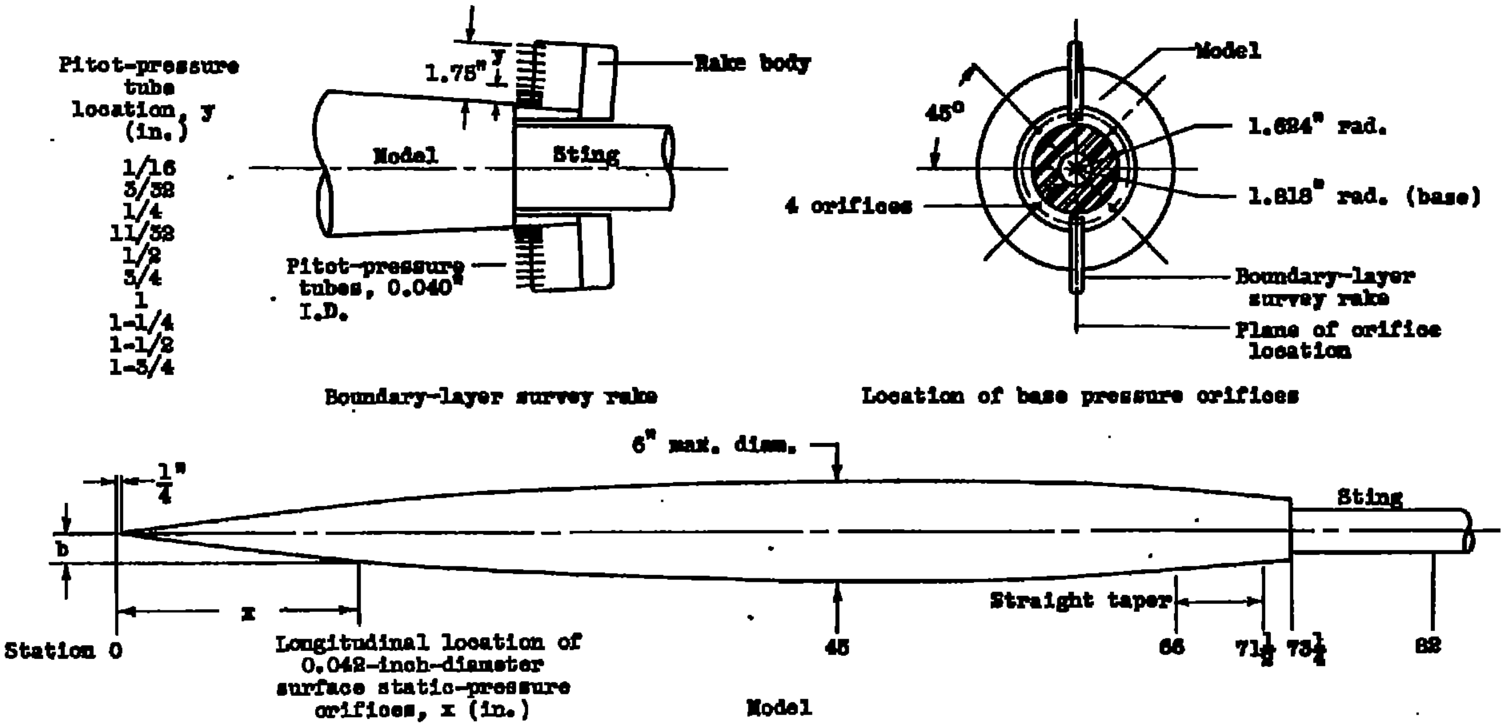

3	$20\frac{1}{2}$	40	58	76
6	$25\frac{3}{4}$	43	61	79
9	28	$46\frac{1}{2}$	64	82
12	31	$49\frac{1}{2}$	67	
15	34	$52\frac{1}{2}$	70	
18	37	$55\frac{1}{2}$	$73\frac{1}{2}$	

Body defined by equations:

$$b = \sqrt{\frac{c}{2}}\ x\left[2 - \frac{x}{45}\right]$$

$$0 \leq x \leq 73.25$$

$$c = \frac{2}{15^2}$$

Figure 1. - Schematic diagram of half-scale model of NACA RM-10 showing boundary-layer survey rake and locations of pressure orifices.

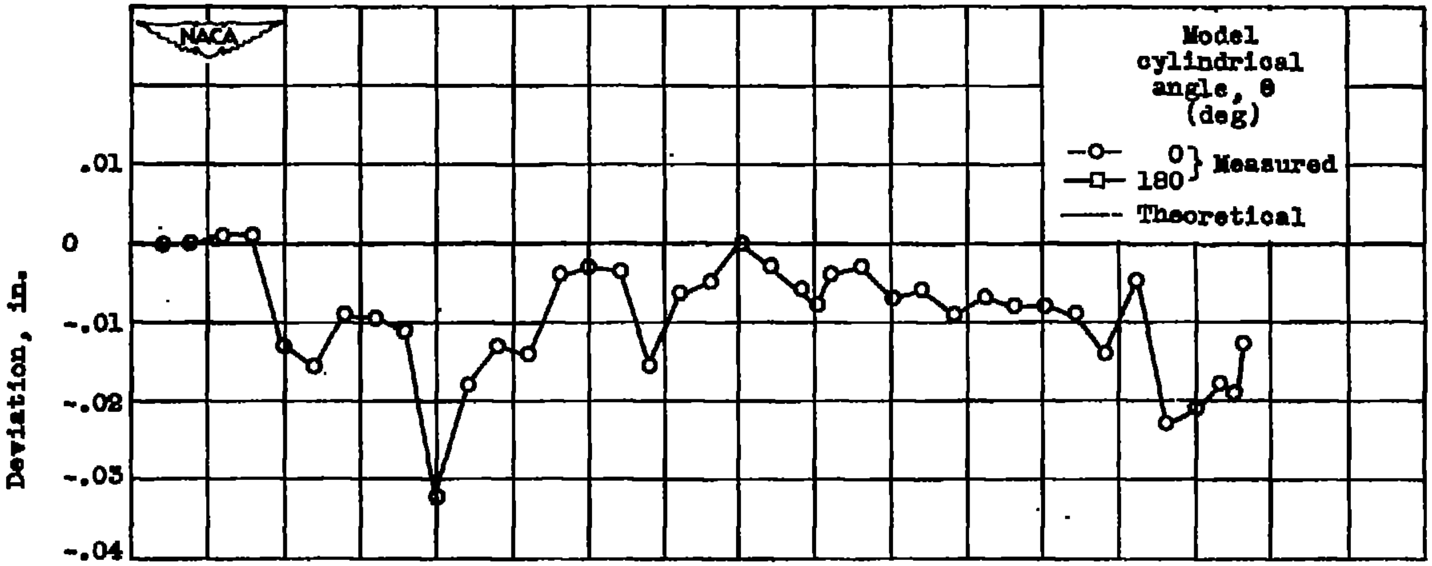

(a) Measured deviation of model ordinates from values calculated from equation (1).

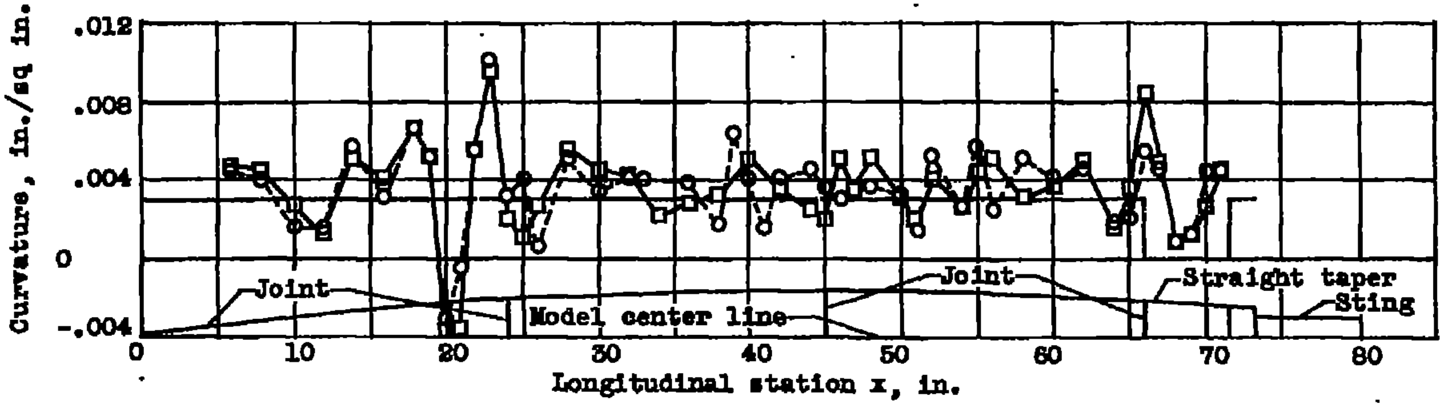

(b) Measured variation of longitudinal model curvature compared with second derivative of equation (1).

Figure 2. - Comparisons of measured model ordinates and longitudinal curvature with their theoretical values at longitudinal stations.

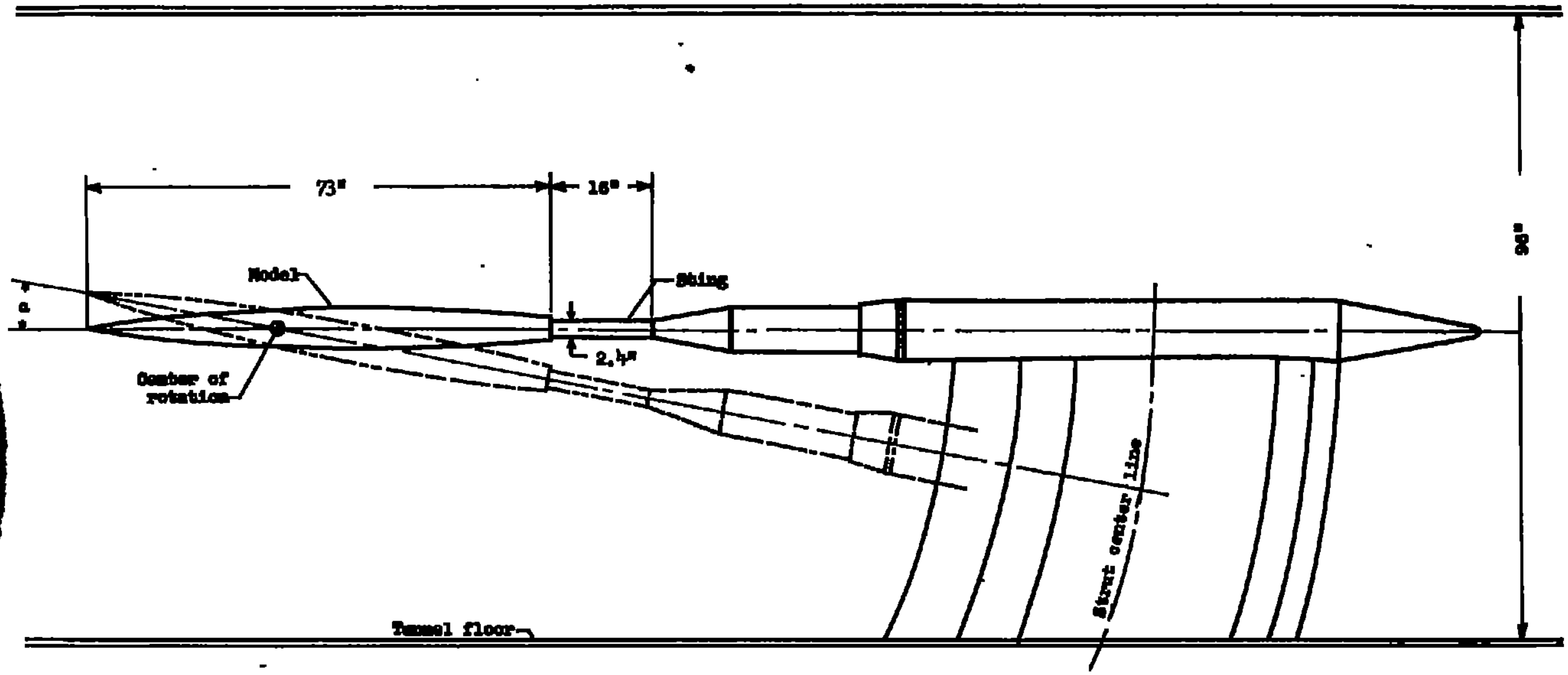

Figure 3. - Installation of model in 8- by 6-foot supersonic wind tunnel.

1296

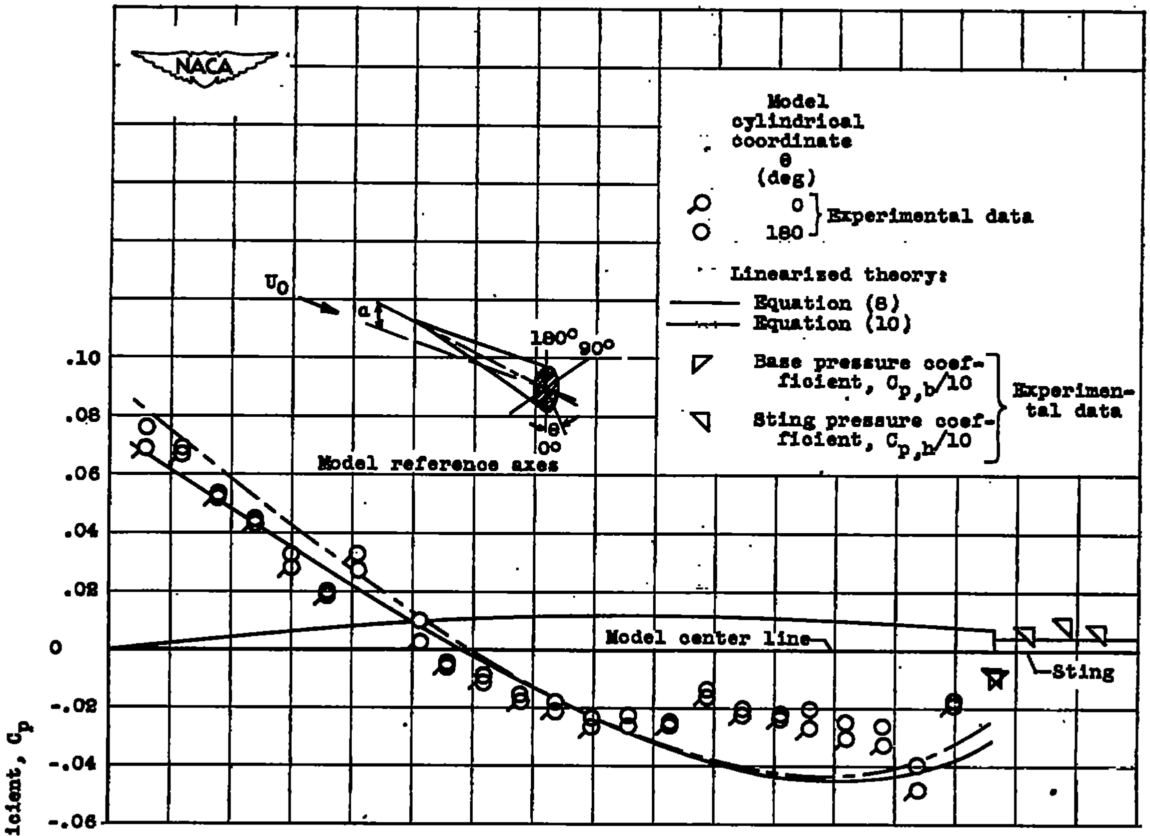

(a) Mach number M_0, 1.49.

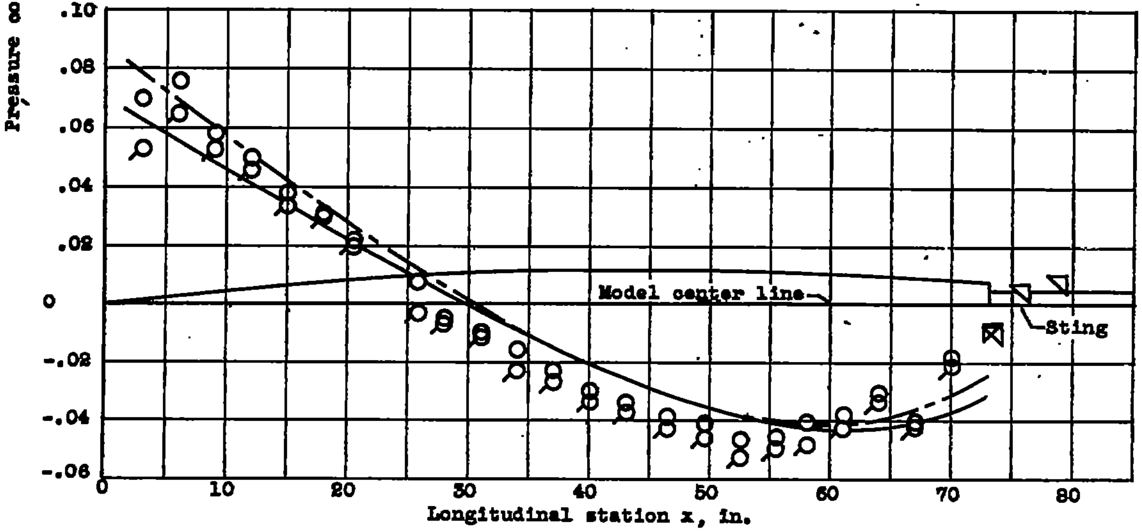

(b) Mach number M_0, 1.59.

Figure 4. - Experimental and theoretical longitudinal variation of pressure coefficient for model at angle of attack of 0°.

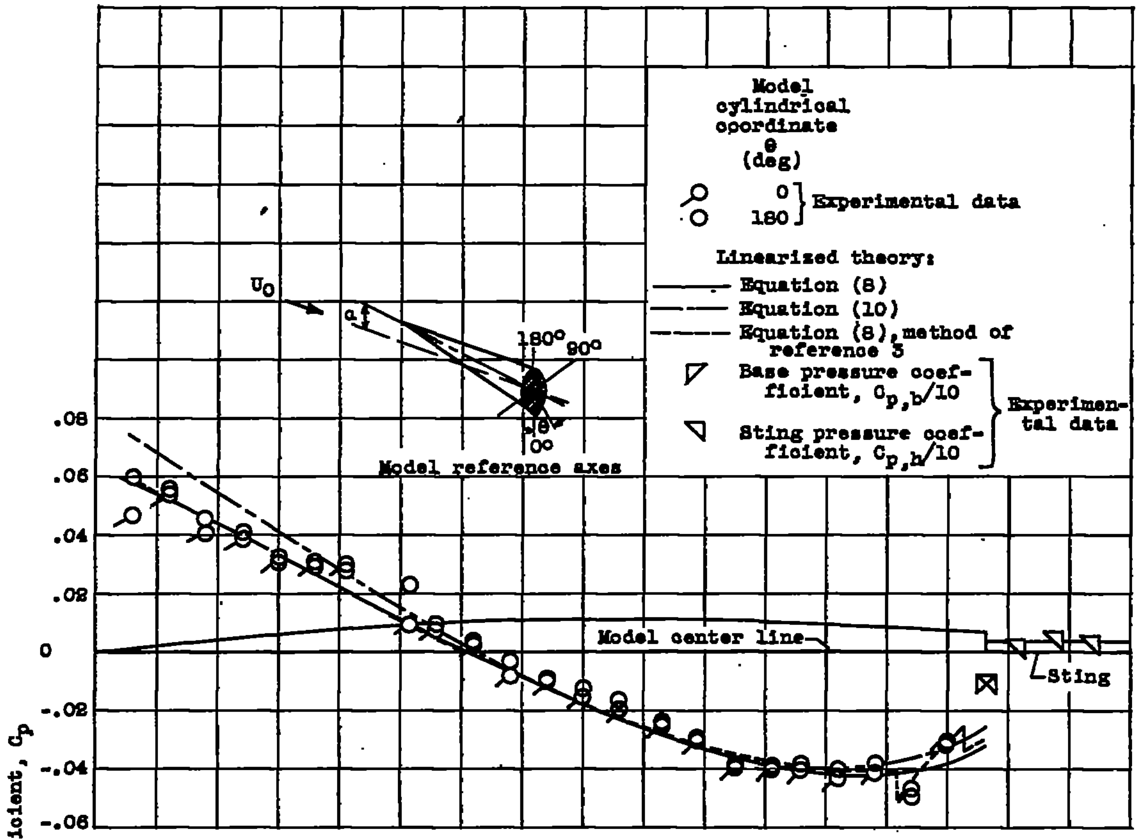

(c) Mach number M_0, 1.78.

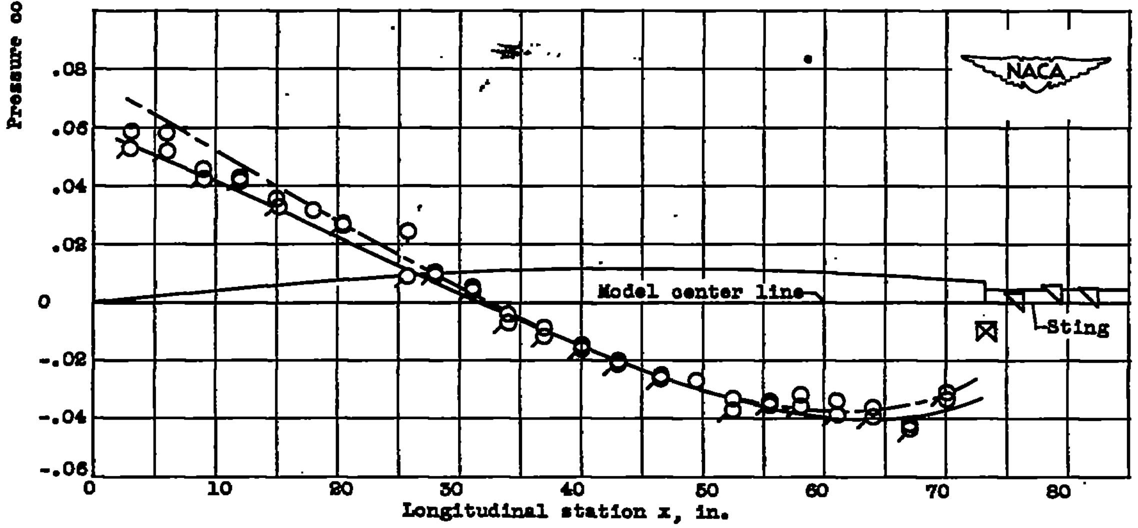

(d) Mach number M_0, 1.98.

Figure 4. - Concluded. Experimental and theoretical longitudinal variation of pressure coefficient for model at angle of attack of 0°.

[redacted]

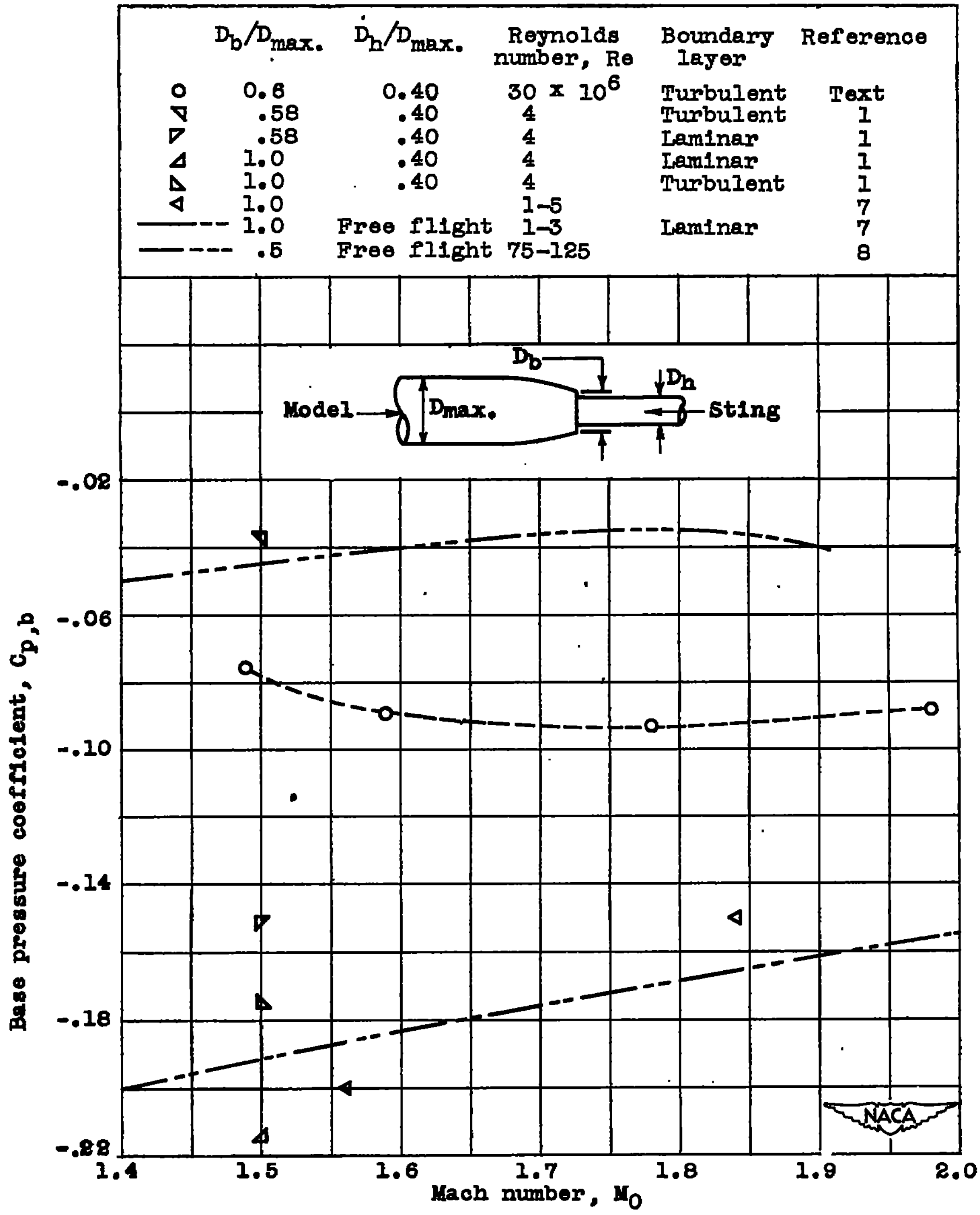

Figure 5. - Experimental variation of base pressure coefficient with Mach number for zero angle of attack. Base pressure coefficients from several references included for comparison.

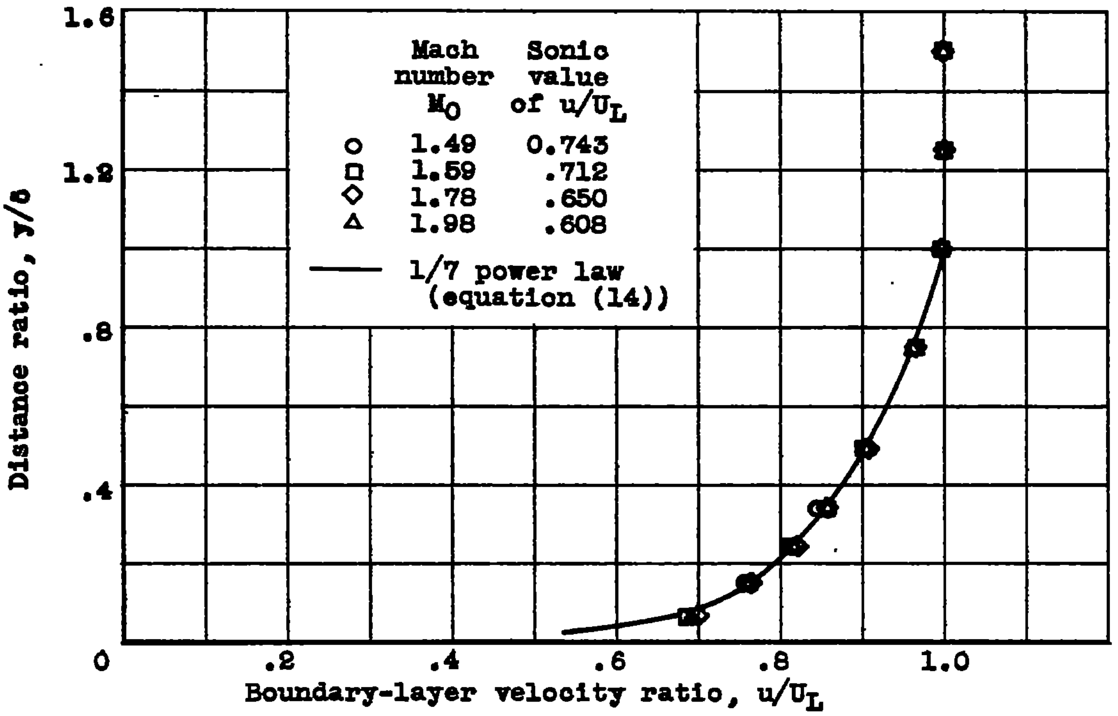

Figure 6. - Experimental and theoretical nondimensional boundary-layer velocity profile for zero angle of attack. Longitudinal station x, $73\frac{1}{4}$ inches.

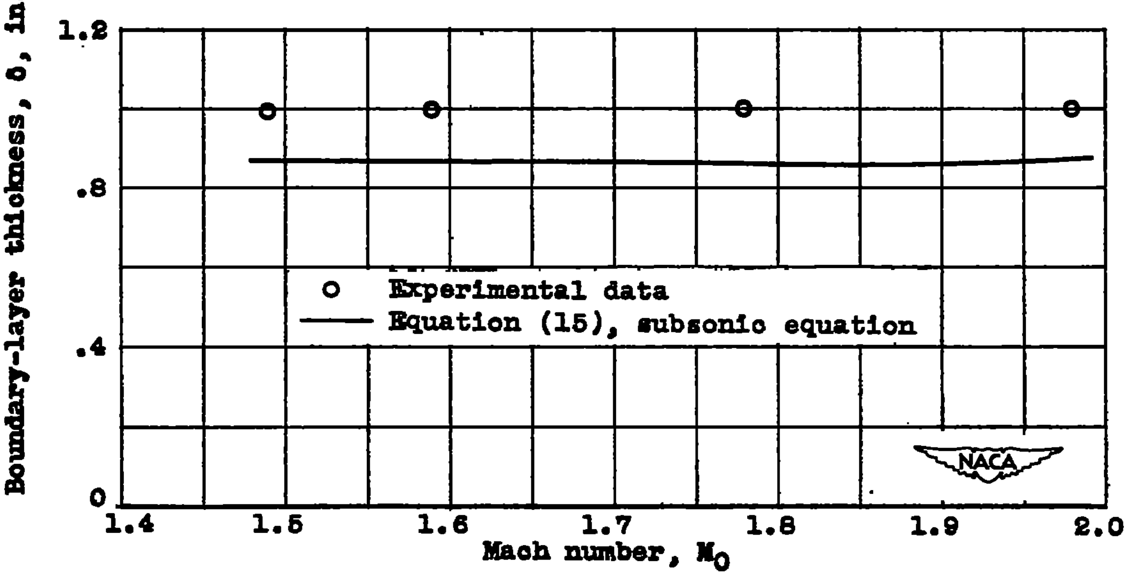

Figure 7. - Experimental and theoretical variation of boundary-layer thickness with Mach number. Angle of attack α, 0°; longitudinal station x, $73\frac{1}{4}$ inches; approximate Reynolds number range, Re, 28 to 31 x 10^6.

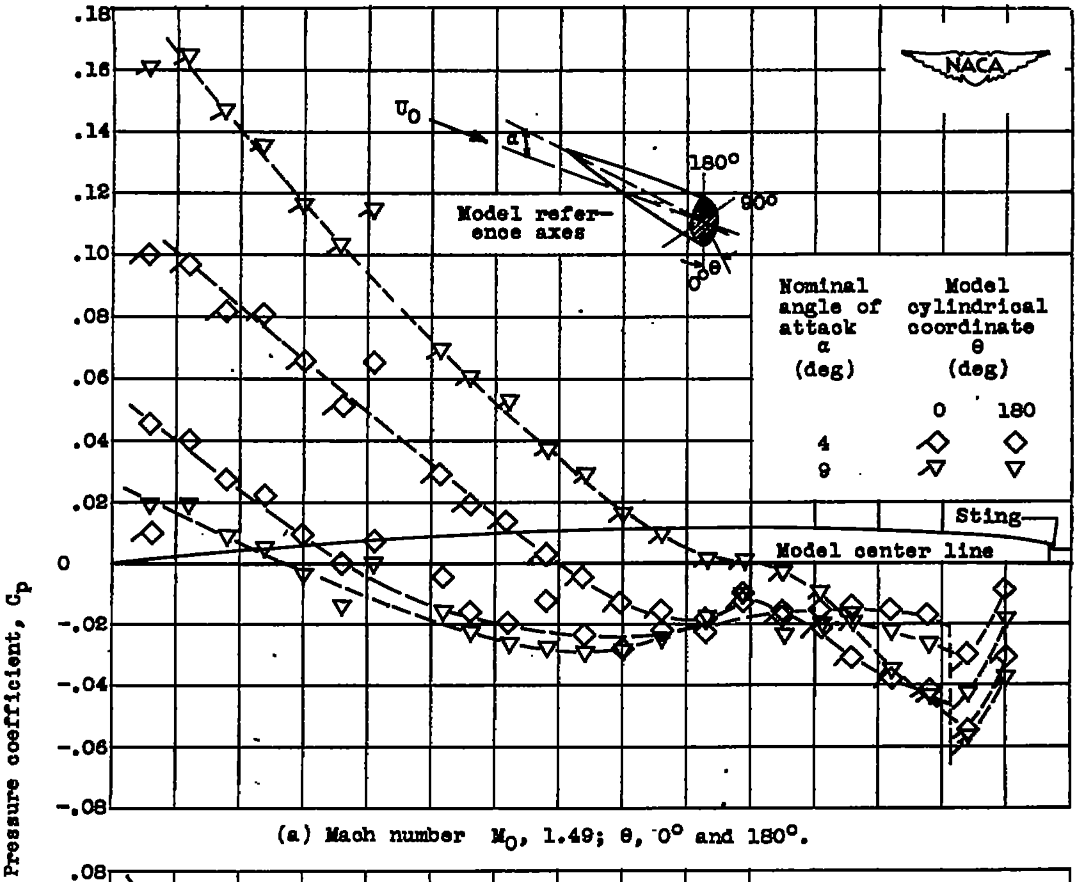

(a) Mach number M_0, 1.49; θ, 0° and 180°.

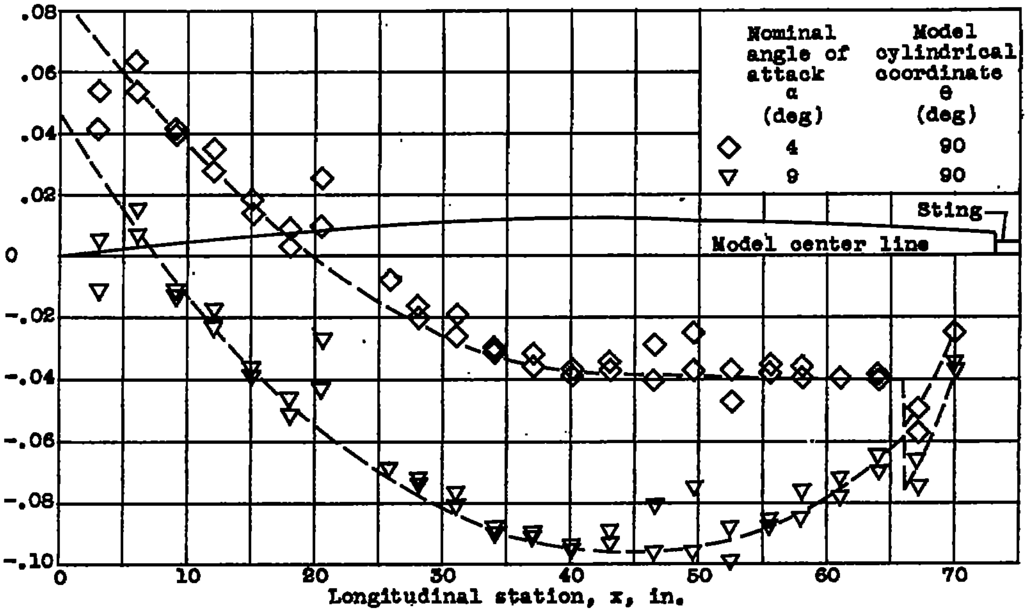

(b) Mach number M_0, 1.49; θ, 90°.

Figure 8. - Experimental longitudinal variation of pressure coefficient for two angles of attack.

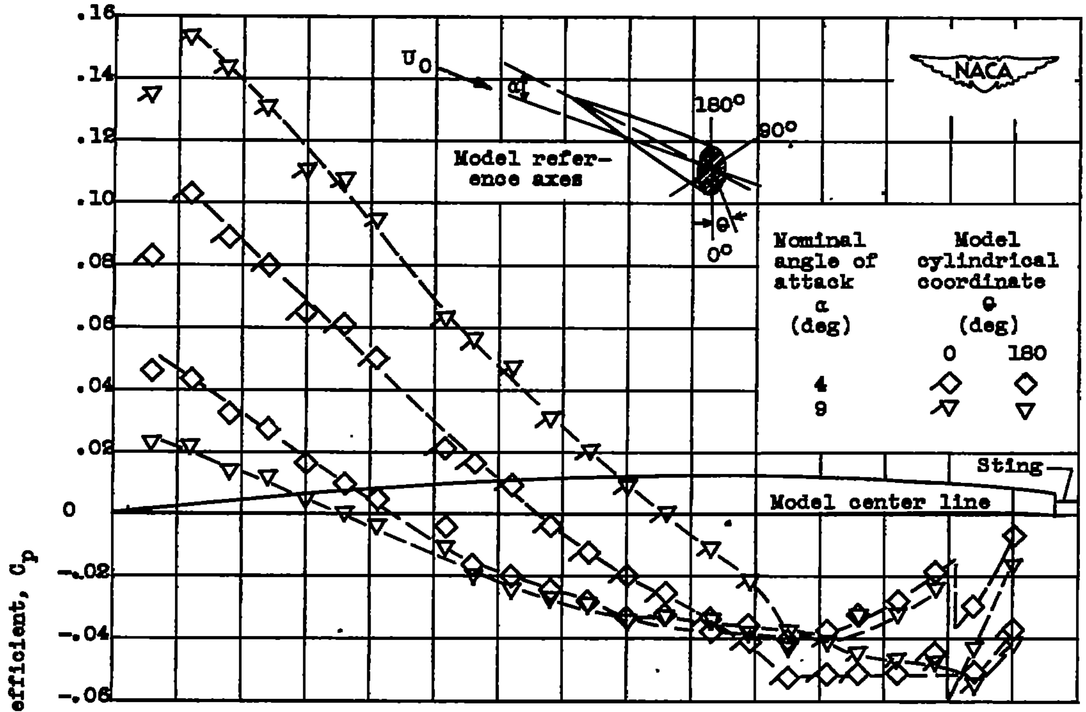

(c) Mach number M , 1.59; θ, 0° and 180°.

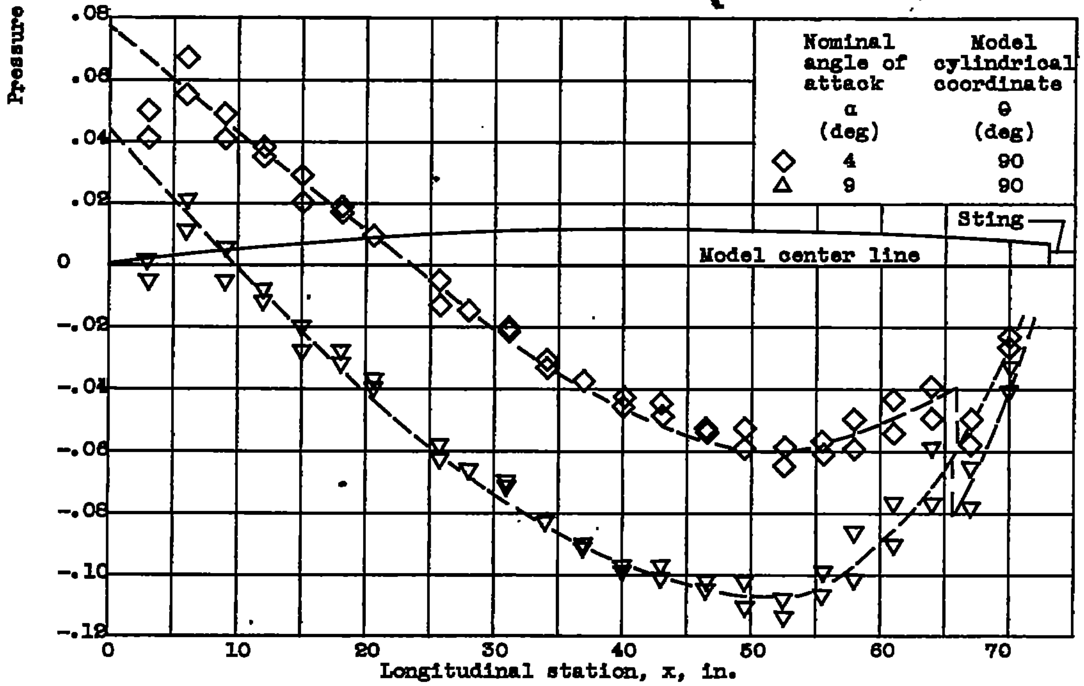

(d) Mach number M_0, 1.59; θ, 90°.

Figure 8. - Continued. Experimental longitudinal variation of pressure coefficient for two angles of attack.

1296

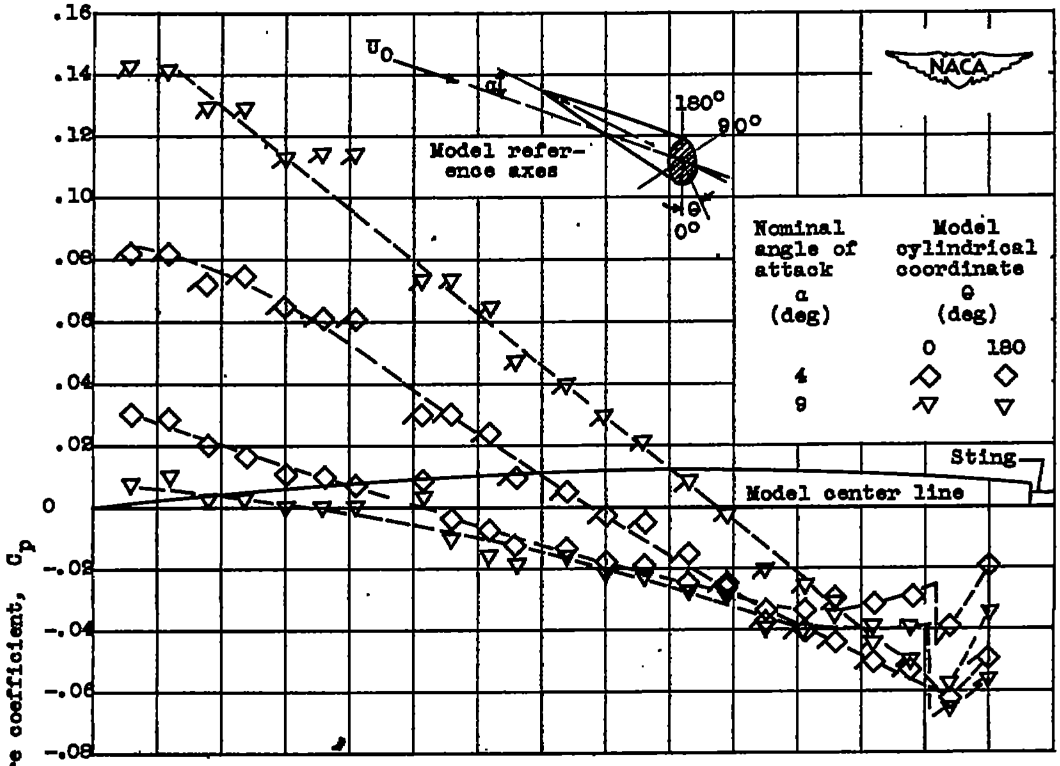

(e) Mach number M_0, 1.78; θ, 0° and 180°.

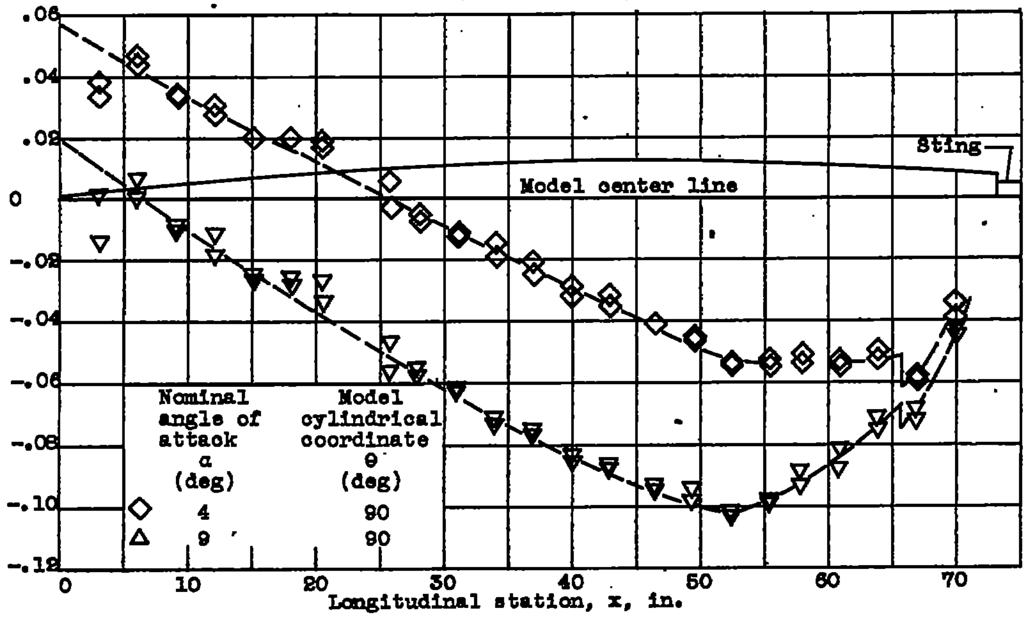

(f) Mach number M_0, 1.78; θ, 90°.

Figure 8. - Continued. Experimental longitudinal variation of pressure coefficient for two angles of attack.

1296

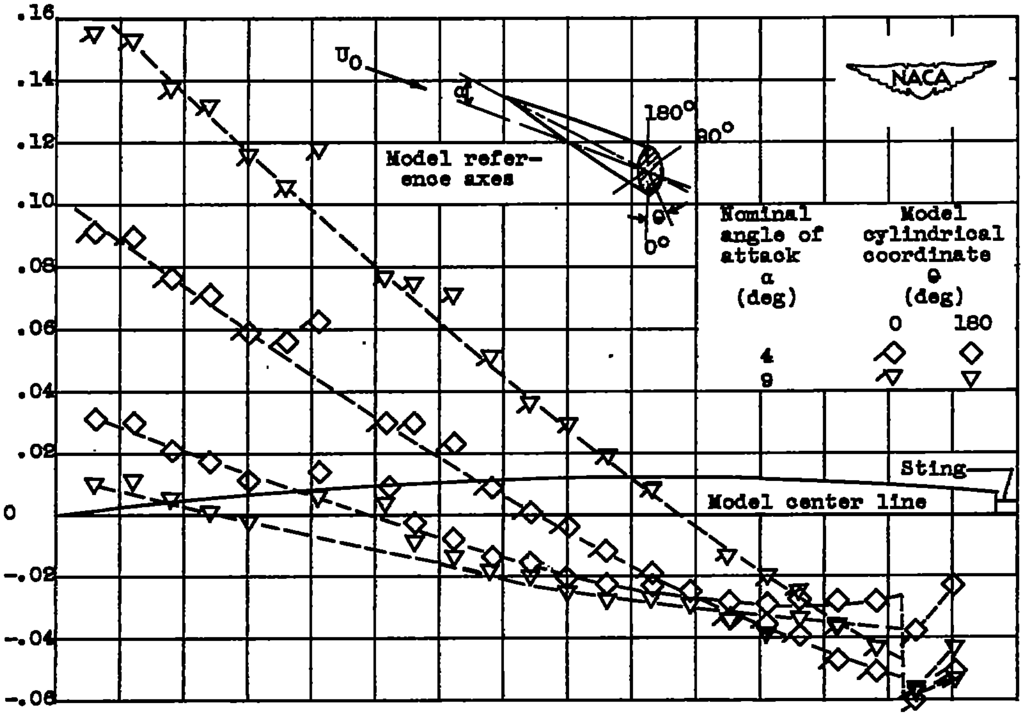

(g) Mach number M_0, 1.98; θ, 0° and 180°.

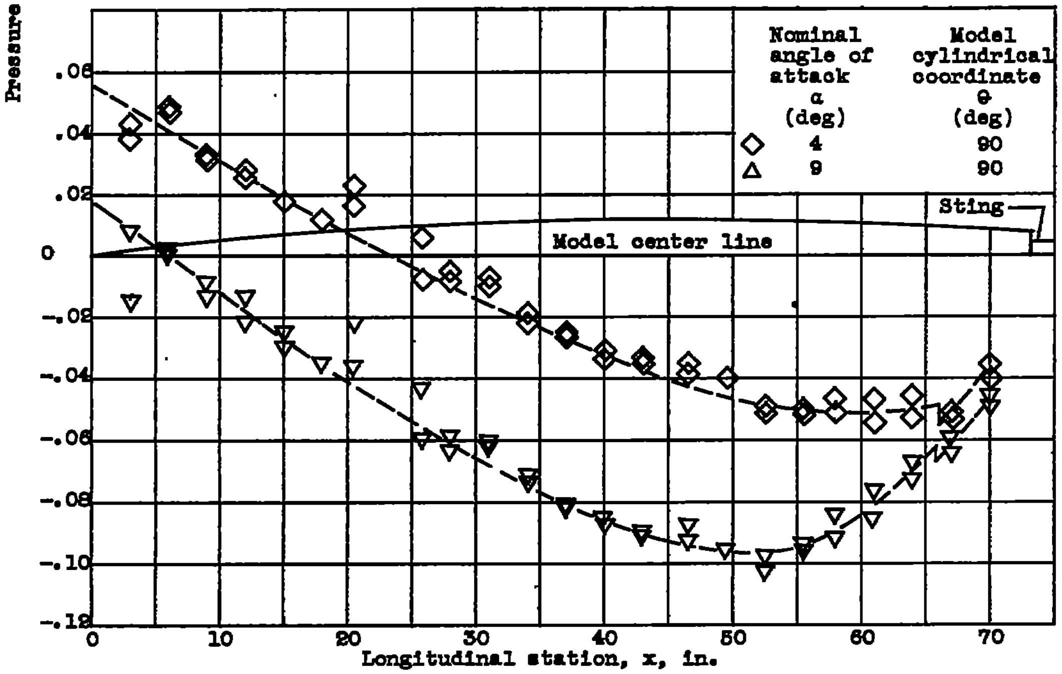

(h) Mach number M_0, 1.98; θ, 90°.

Figure 8. - Concluded. Experimental longitudinal variation of pressure coefficient for two angles of attack.

[redacted]

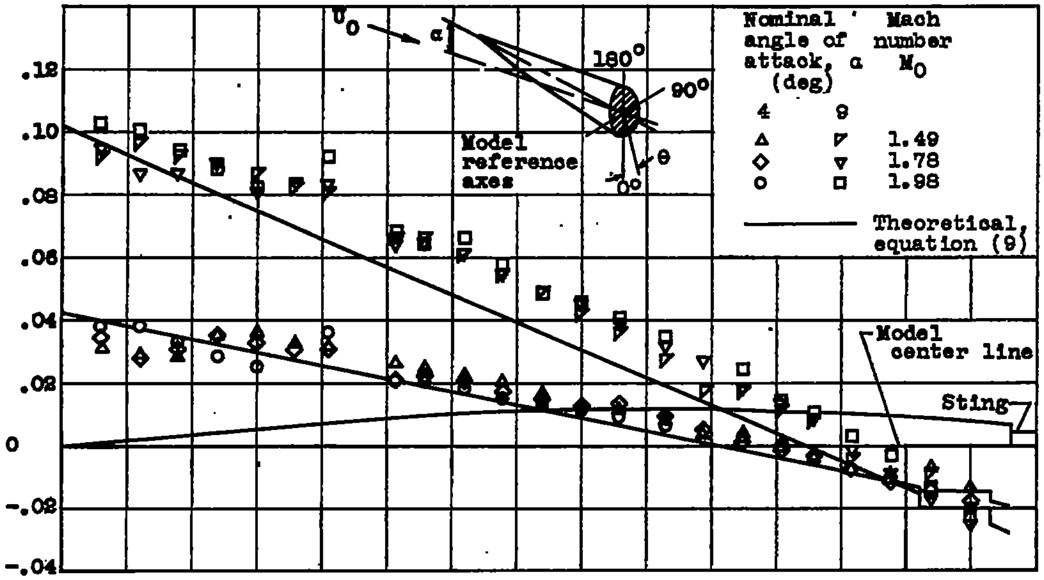

(a) Windward side of model; θ, 0°.

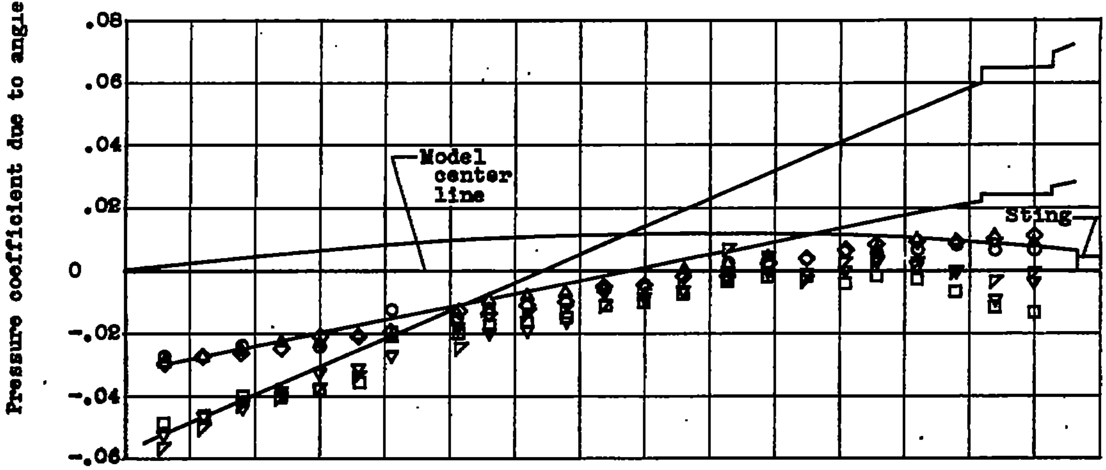

(b) Leeward side of model; θ, 180°.

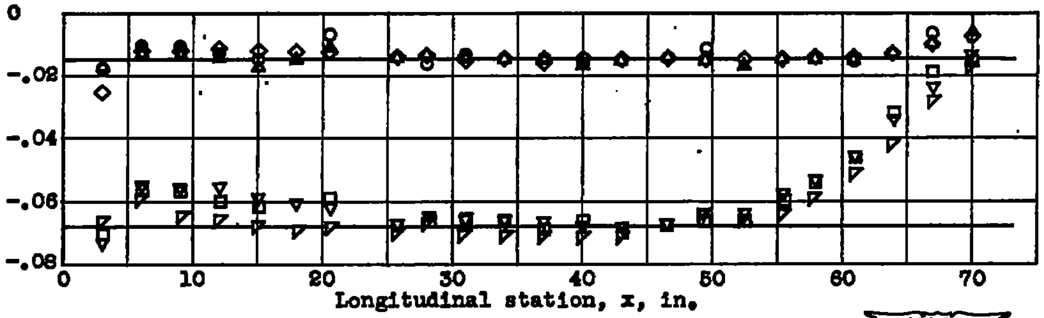

(c) Side of model; θ, 90°.

Figure 9. - Experimental and theoretical longitudinal variation of pressure coefficient due to angle of attack for two angles of attack and several Mach numbers.

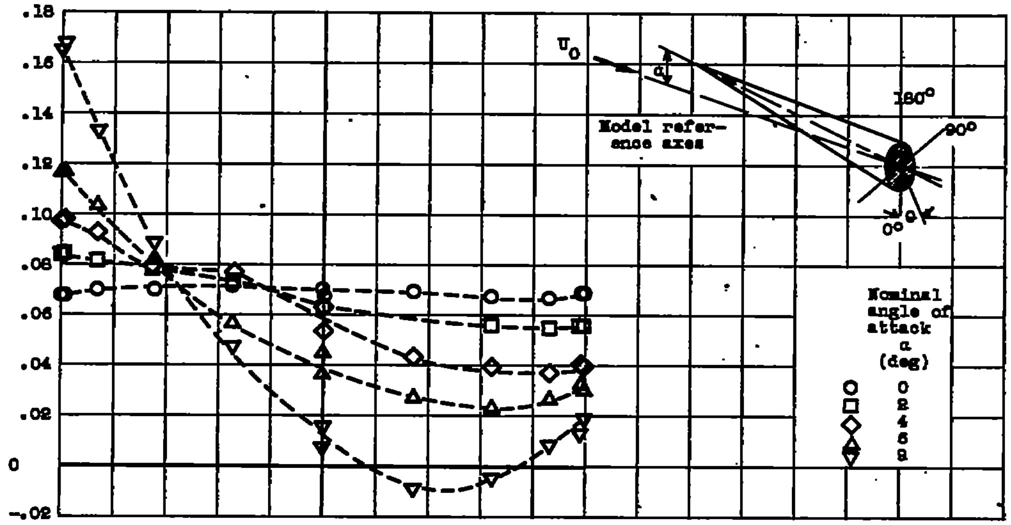

(a) Longitudinal station x, 6 inches.

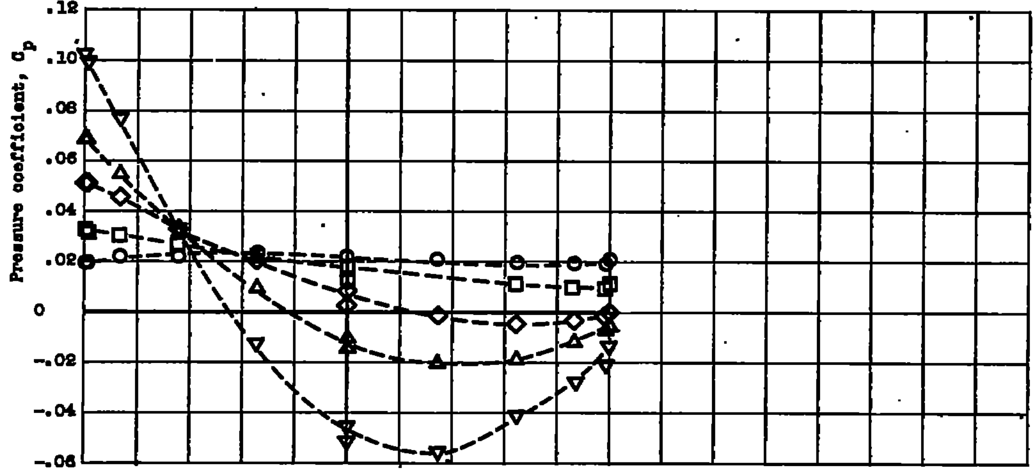

(b) Longitudinal station x, 18 inches.

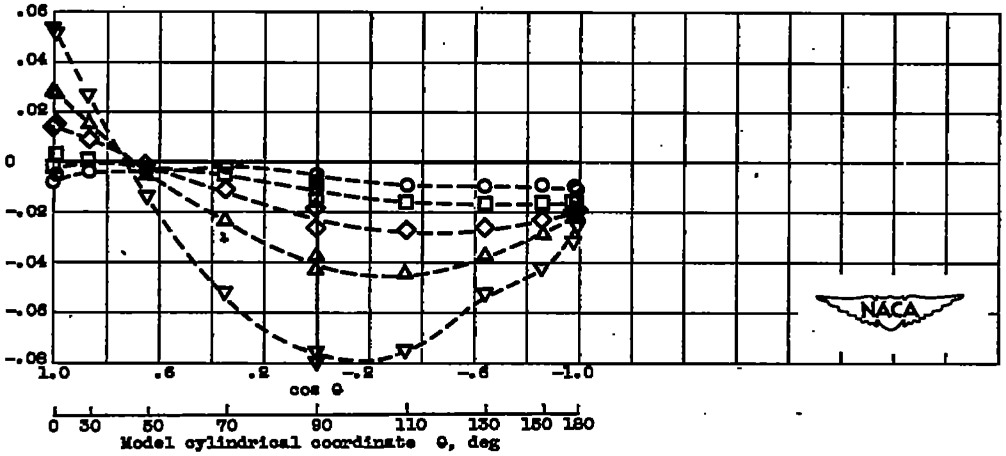

(c) Longitudinal station x, 31 inches.

Figure 10. - Experimental variation of pressure coefficient with angular positions on body. Mach number M_0, 1.49.

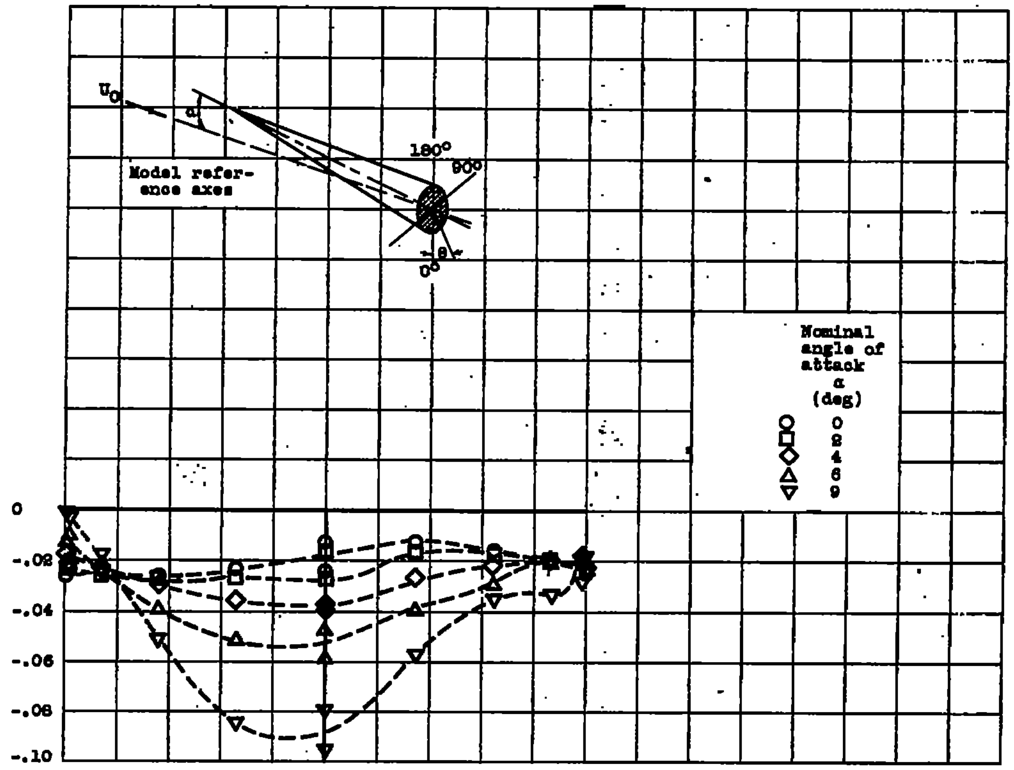

(d) Longitudinal station x, $46\frac{1}{8}$ inches.

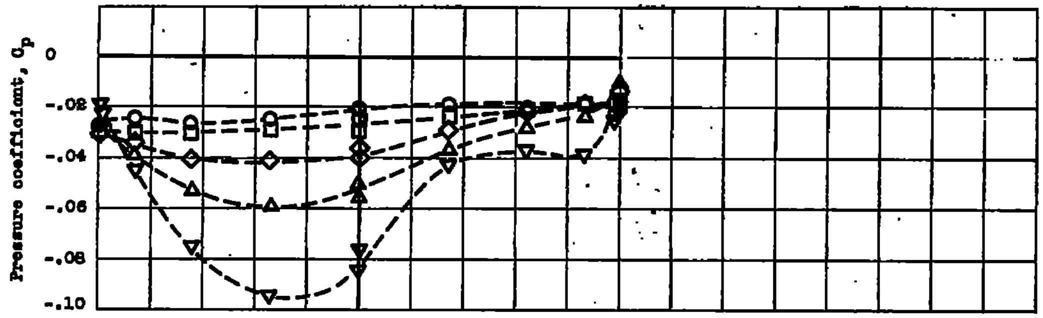

(e) Longitudinal station x, 58 inches.

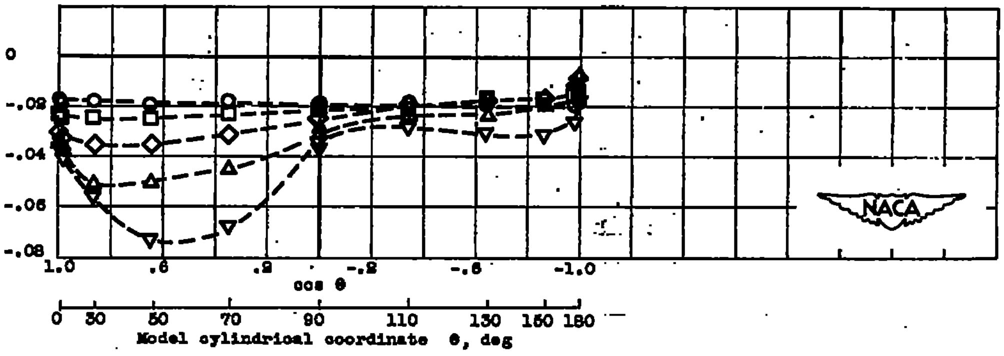

(f) Longitudinal station x, 70 inches.

Figure 10. - Concluded. Experimental variation of pressure coefficient with angular positions on body. Mach number M_0, 1.49.

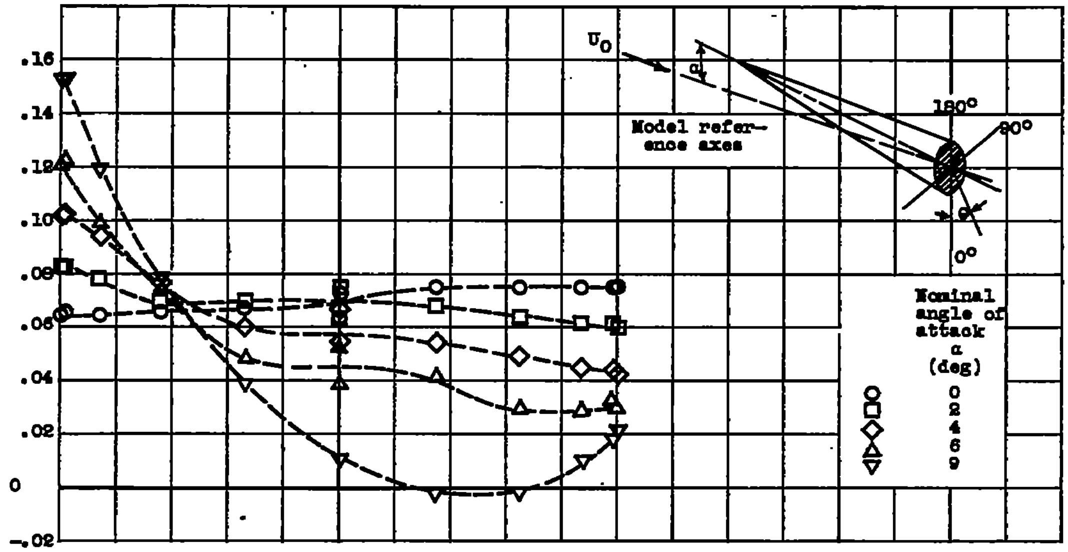

(a) Longitudinal station x, 6 inches.

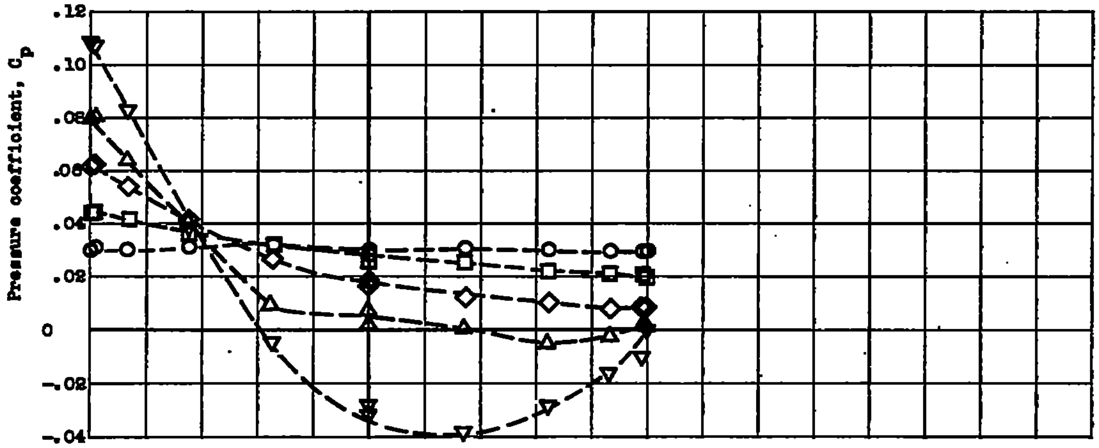

(b) Longitudinal station x, 18 inches.

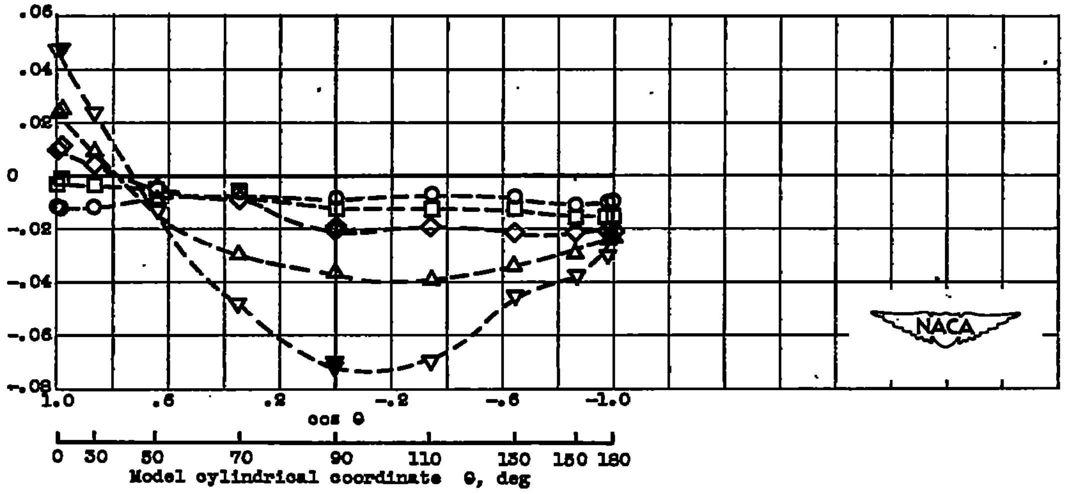

(c) Longitudinal station x, 31 inches.

Figure 11. - Experimental variation of pressure coefficient with angular positions on body. Mach number M_0, 1.59.

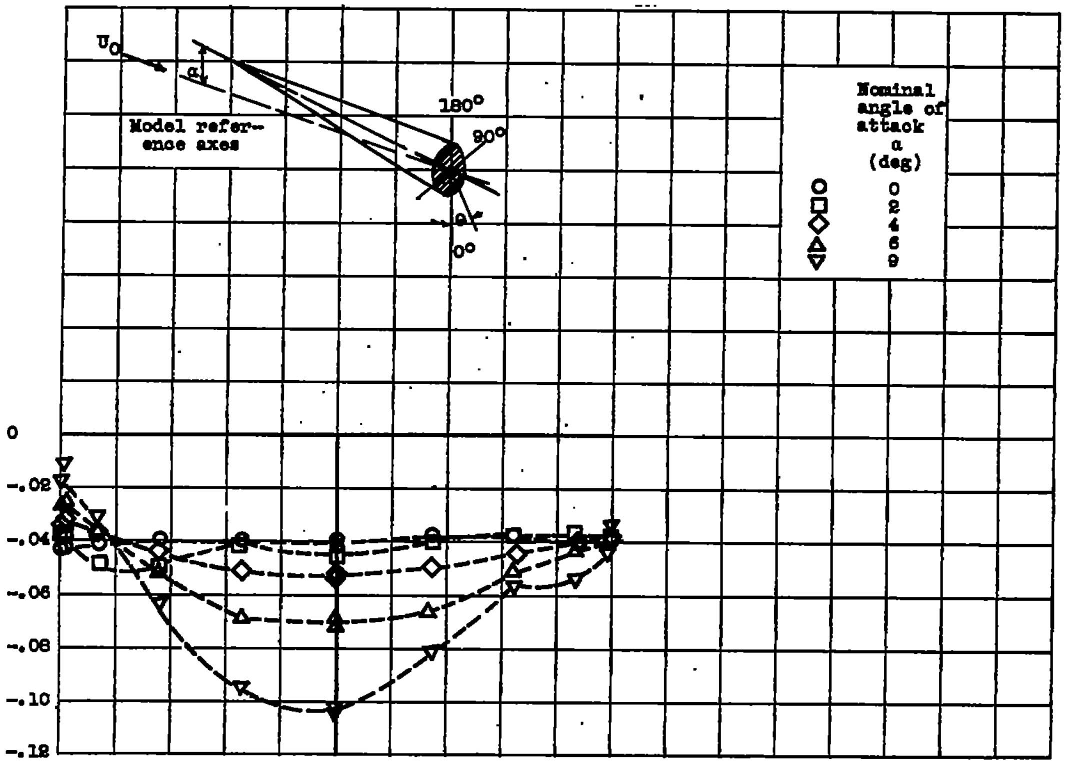

(d) Longitudinal station x, $46\frac{1}{2}$ inches.

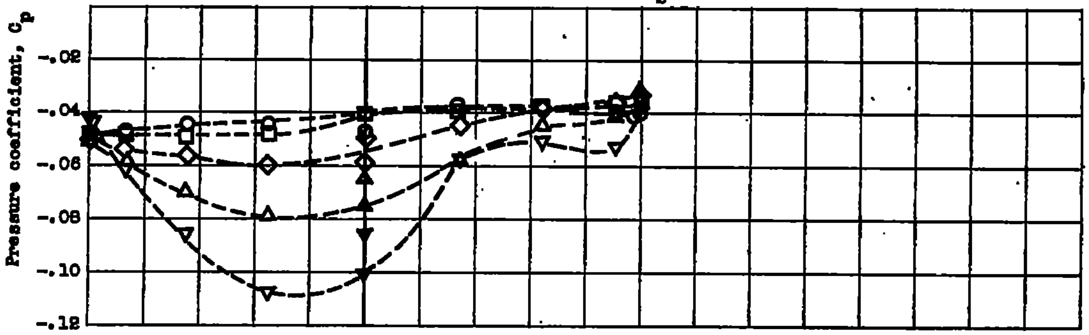

(e) Longitudinal station x, 58 inches.

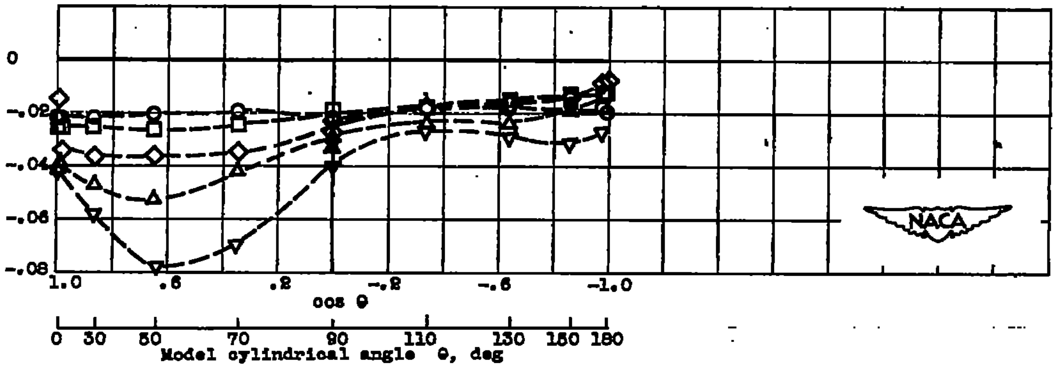

(f) Longitudinal station x, 70 inches.

Figure 11. - Concluded. Experimental variation of pressure coefficient with angular positio on body. Mach number M_0, 1.59.

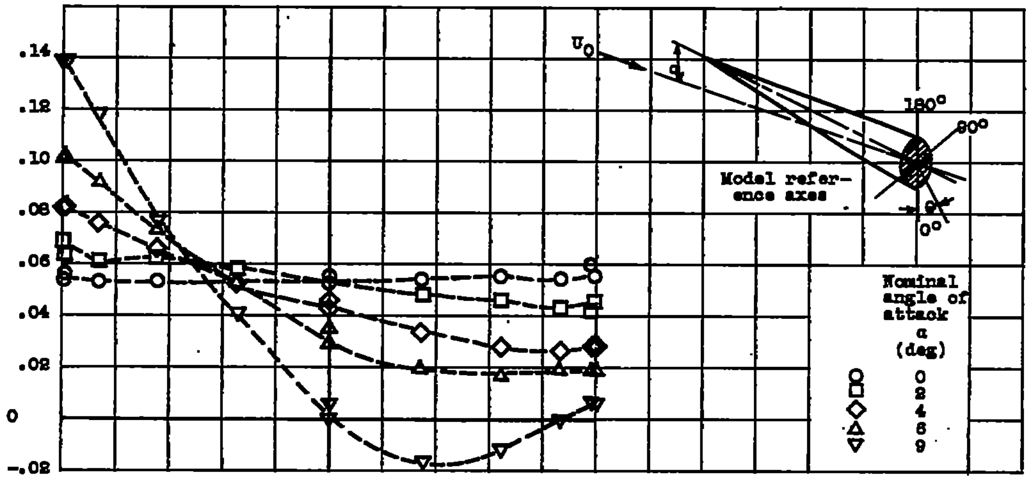

(a) Longitudinal station x, 6 inches.

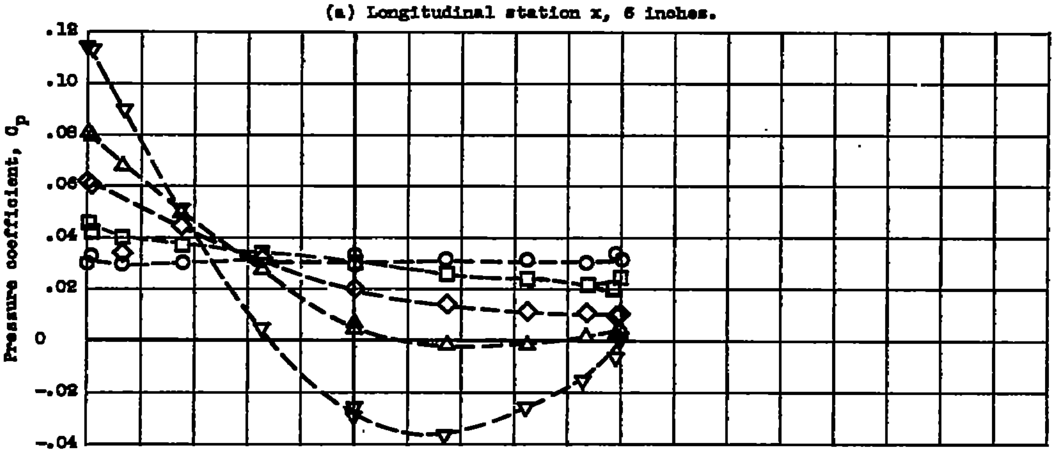

(b) Longitudinal station x, 18 inches.

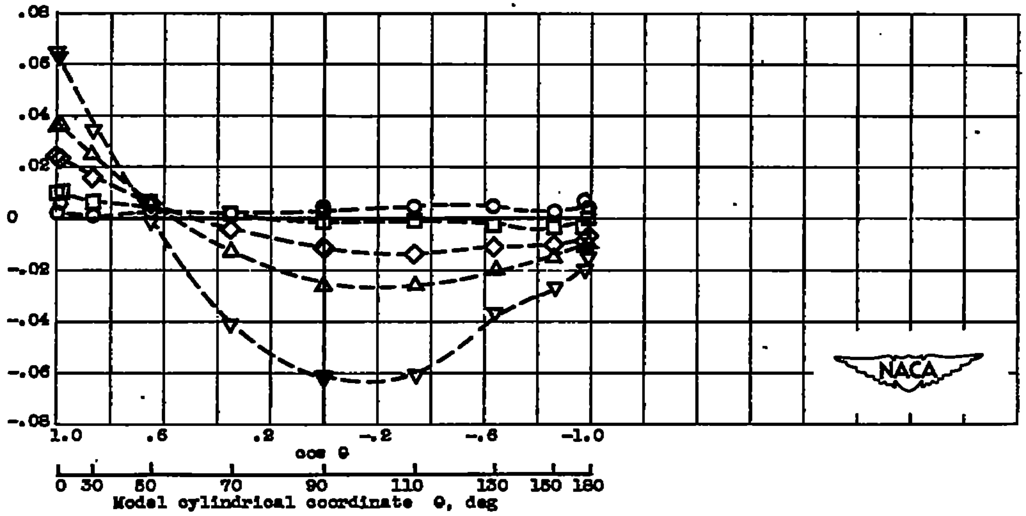

(c) Longitudinal station x, 31 inches.

Figure 12. - Experimental variation of pressure coefficient with angular positions on body. Mach number M_0, 1.78.

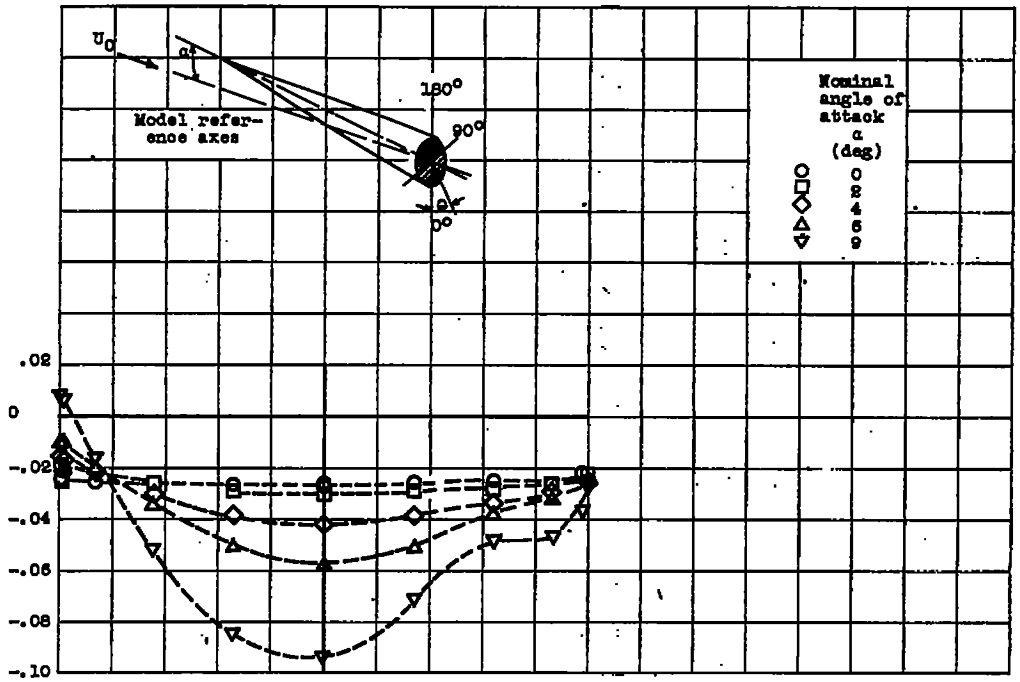

(d) Longitudinal station x, $46\frac{1}{2}$ inches.

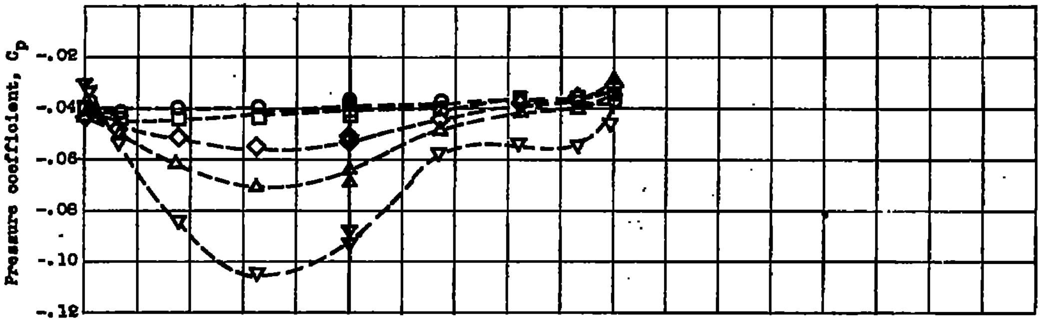

(e) Longitudinal station x, 58 inches.

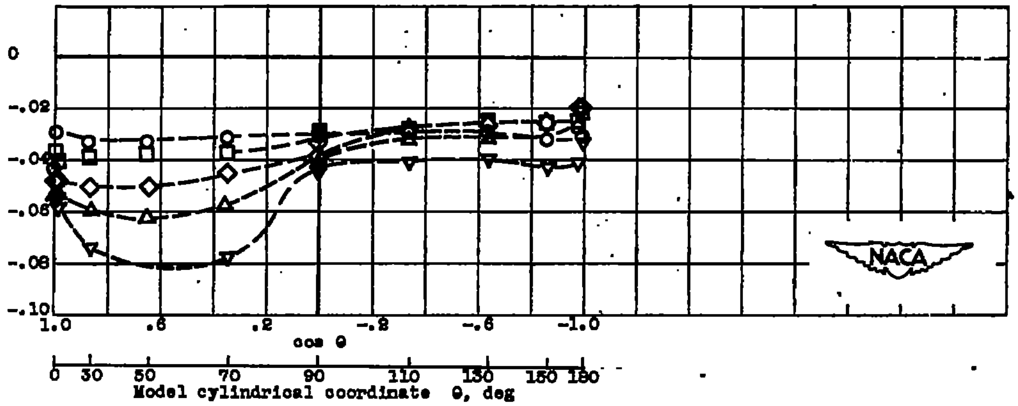

(f) Longitudinal station x, 70 inches.

Figure 12. - Concluded. Experimental variation of pressure coefficient with angular positions on body. Mach number M_0, 1.78.

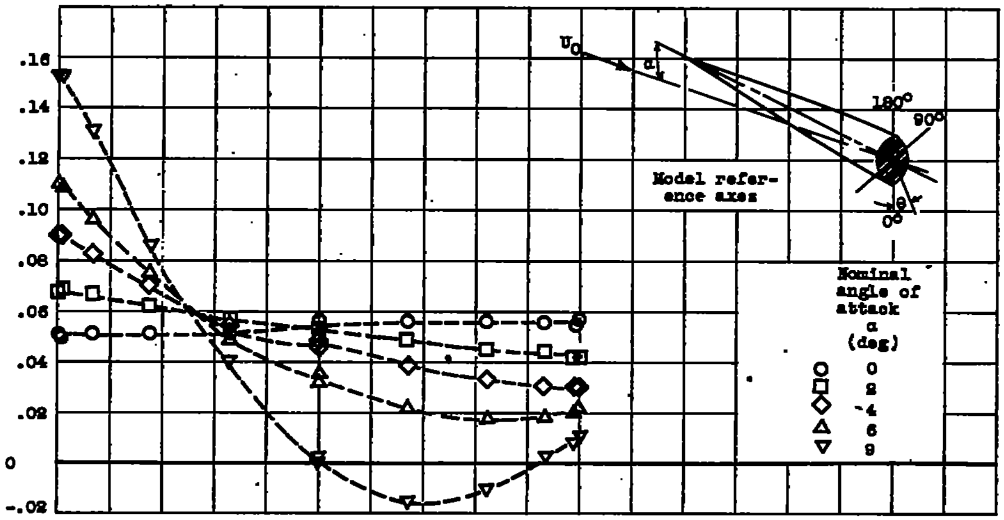

(a) Longitudinal station x, 6 inches.

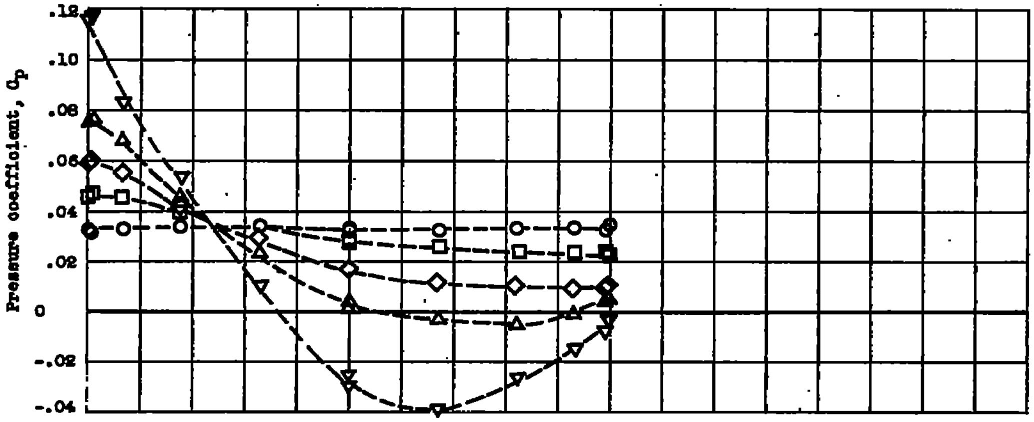

(b) Longitudinal station x, 15 inches.

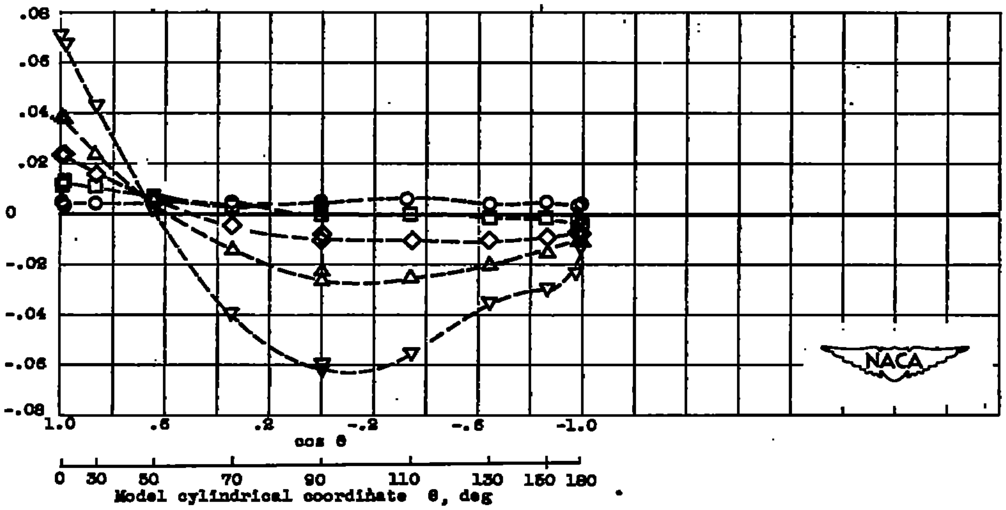

(c) Longitudinal station x, 31 inches.

Figure 13. - Experimental variation of pressure coefficient with angular positions on body. Mach number M_0, 1.98.

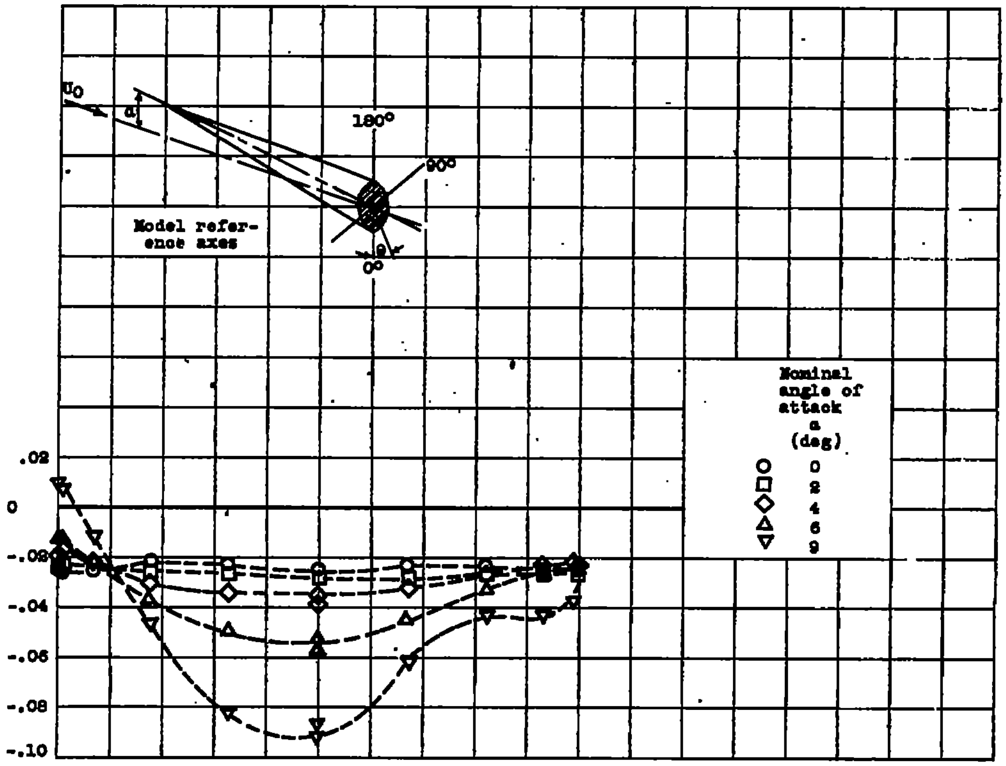

(d) Longitudinal station x, $46\frac{1}{2}$ inches.

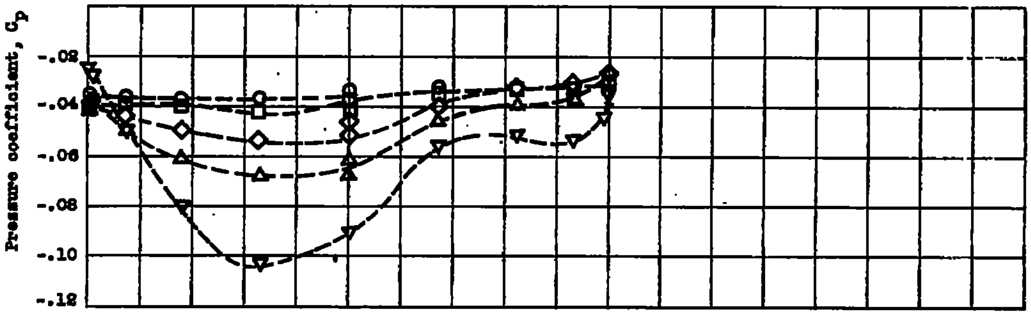

(e) Longitudinal station x, 58 inches.

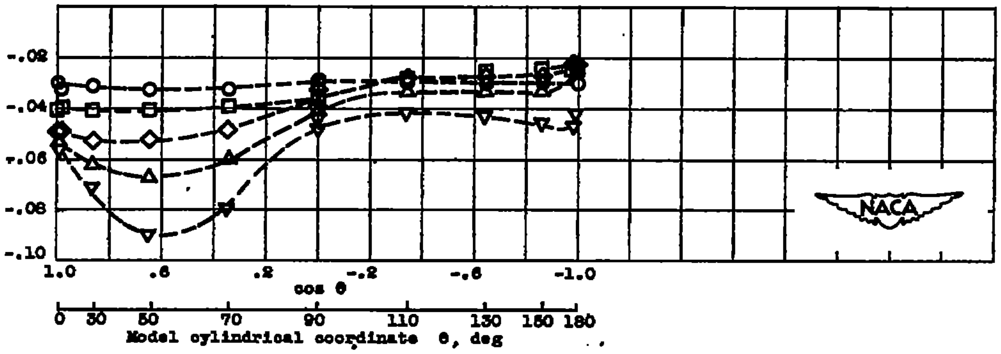

(f) Longitudinal station x, 70 inches.

Figure 13. - Concluded. Experimental variation of pressure coefficient with angular positions on body. Mach number M_0, 1.49.

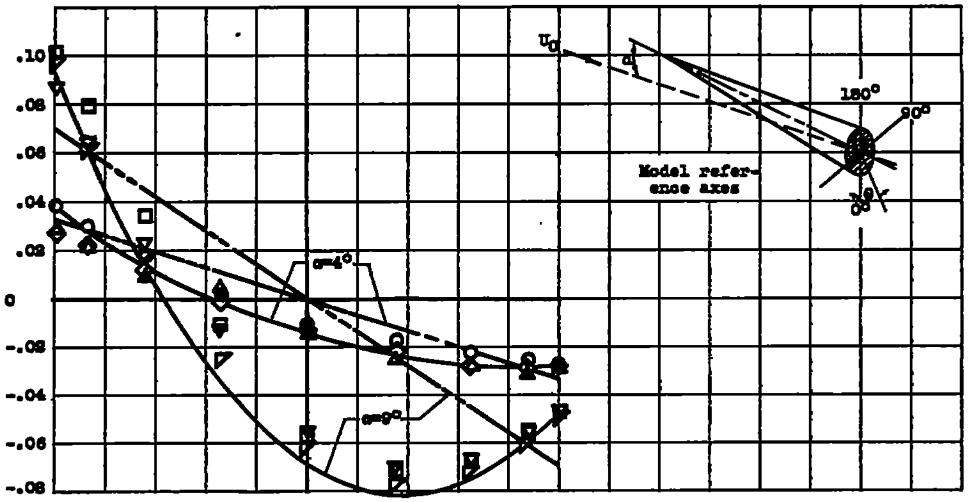

(a) Longitudinal station x, 6 inches.

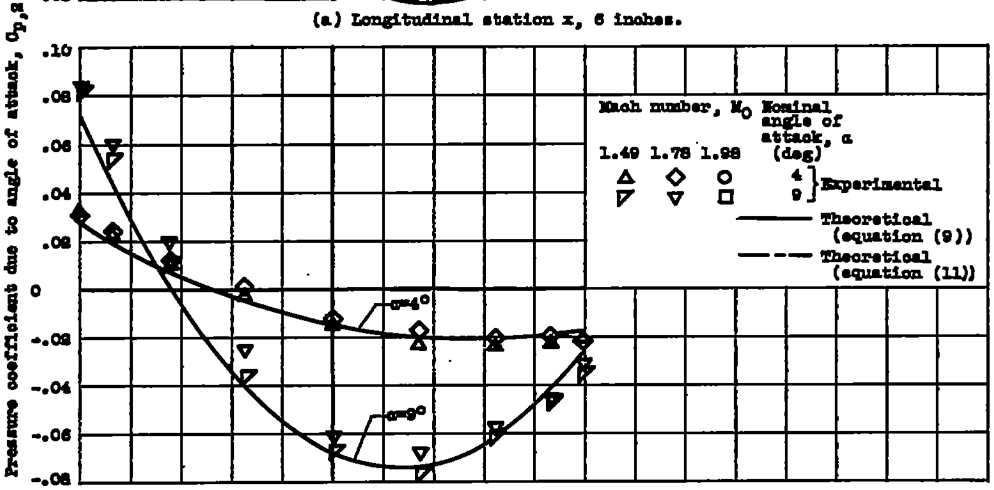

(b) Longitudinal station x, 18 inches.

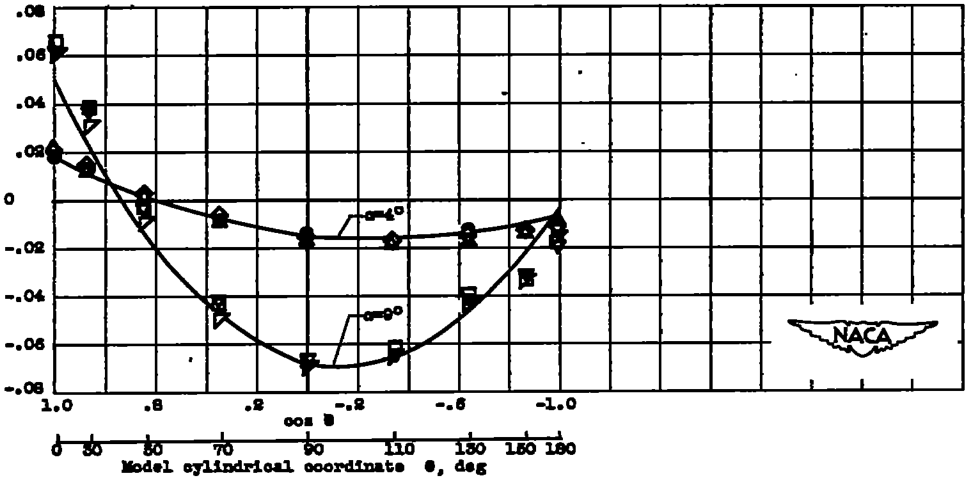

(c) Longitudinal station x, 31 inches.

Figure 14. - Theoretical and experimental variation of pressure coefficient due to angle of attack with angular positions on body for two angles of attack and several Mach numbers.

[redacted]

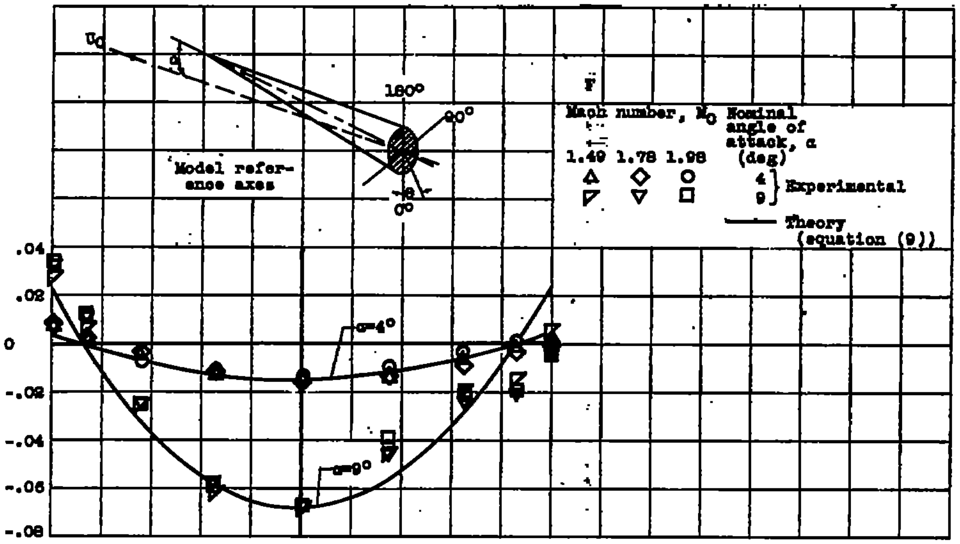

(d) Longitudinal station x, $46\frac{1}{8}$ inches.

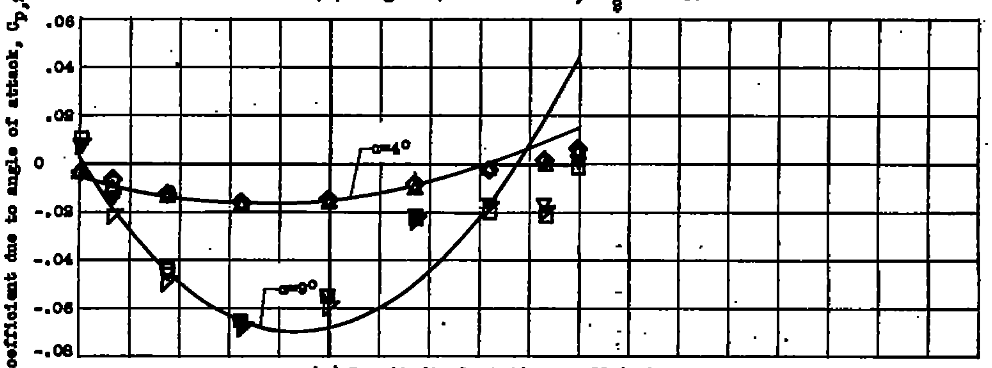

(e) Longitudinal station x, 58 inches.

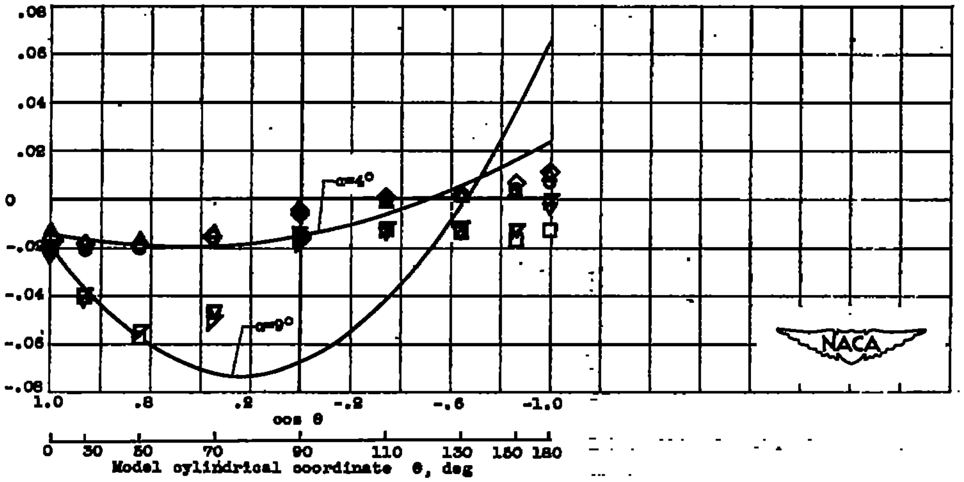

(f) Longitudinal station x, 70 inches.

Figure 14. - Concluded. Theoretical and experimental variation of pressure coefficient due to angle of attack with angular positions on body for two angles of attack and several Mach numbers.

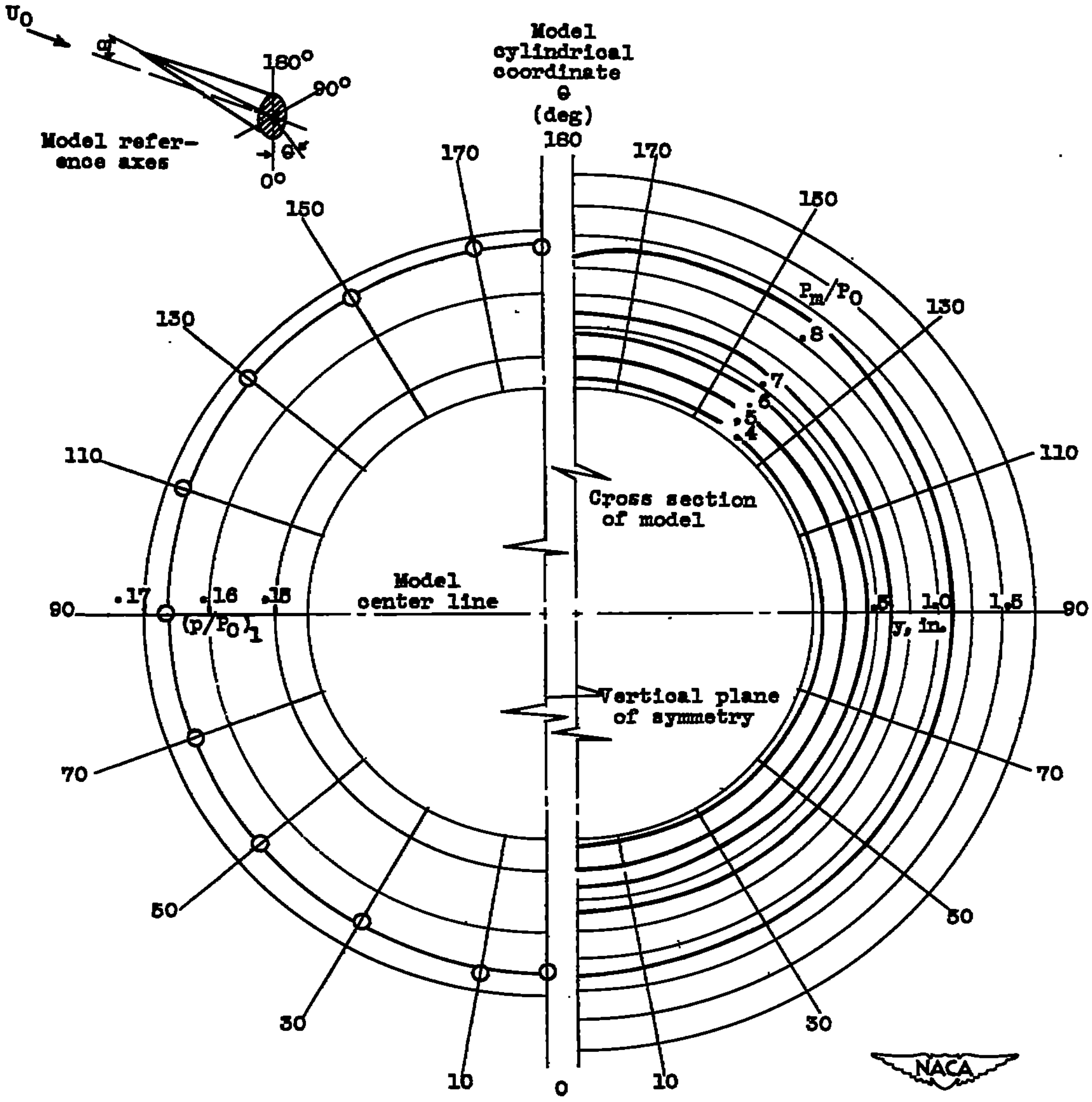

x, 70 inches; free-stream pressure ratio p_0/P_0, 0.179.

x, $73\frac{1}{4}$ inches; free-stream total-pressure ratio $P_{m,0}/P_0$, 0.821.

(a) Angle of attack α, 0°.

Figure 15. - Experimental variation of ratio of static to free-stream total pressure p/P_0 on body surface and ratio of pitot to free-stream total pressure P_m/P_0 in flow field at rear of model. Mach number M_0, 1.78.

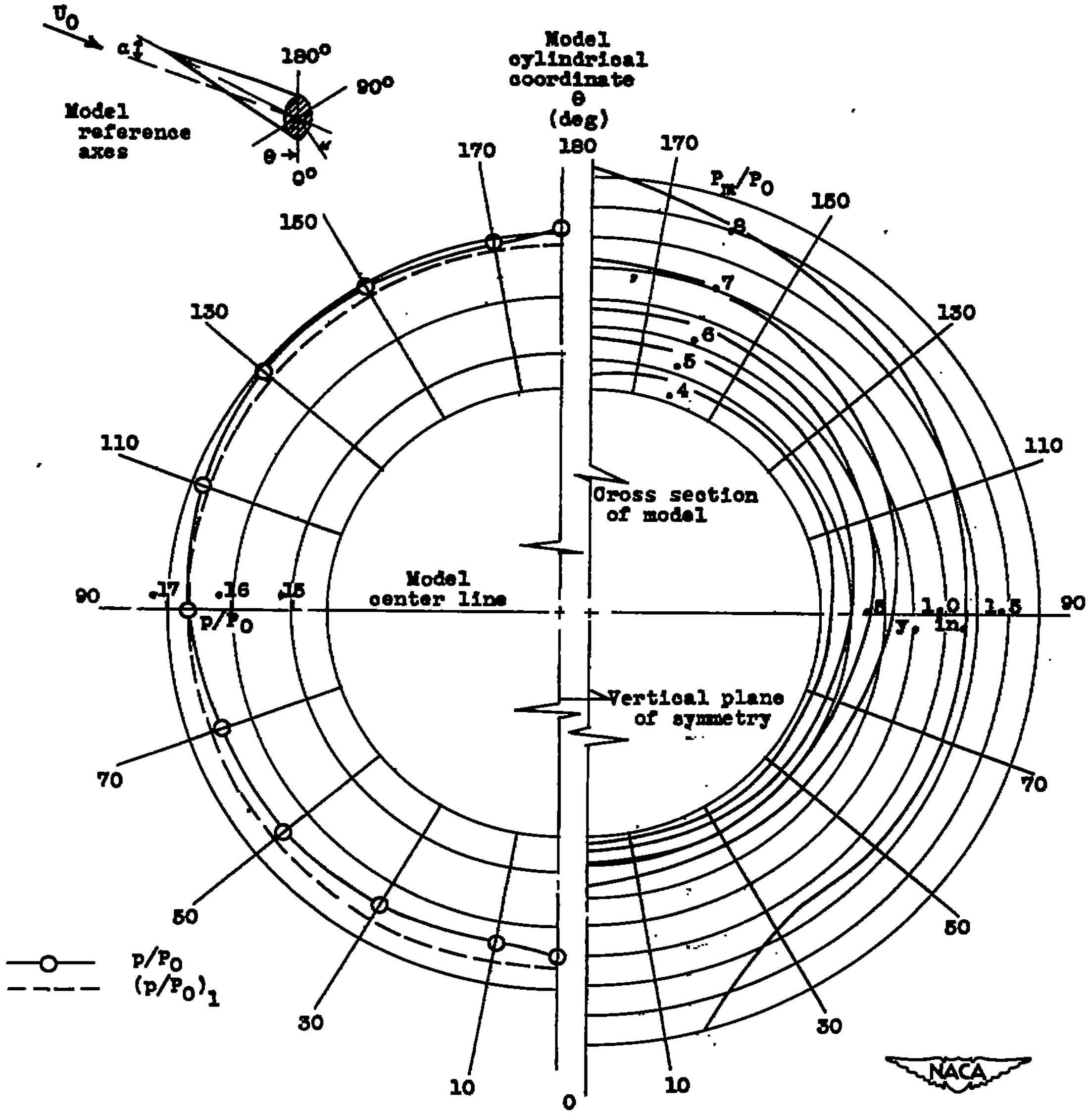

x, 70 inches; free-stream pressure ratio p_0/P_0, 0.179.

x, $73\frac{1}{4}$ inches; free-stream total-pressure ratio $P_{m,0}/P_0$, 0.821.

(b) Angle of attack α, 2°.

Figure 15. - Continued. Experimental variation of ratio of static to free-stream total pressure p/P_0 on body surface and ratio of pitot to free-stream total pressure P_m/P_0 in flow field at rear of model. Mach number M_0, 1.78.

1296

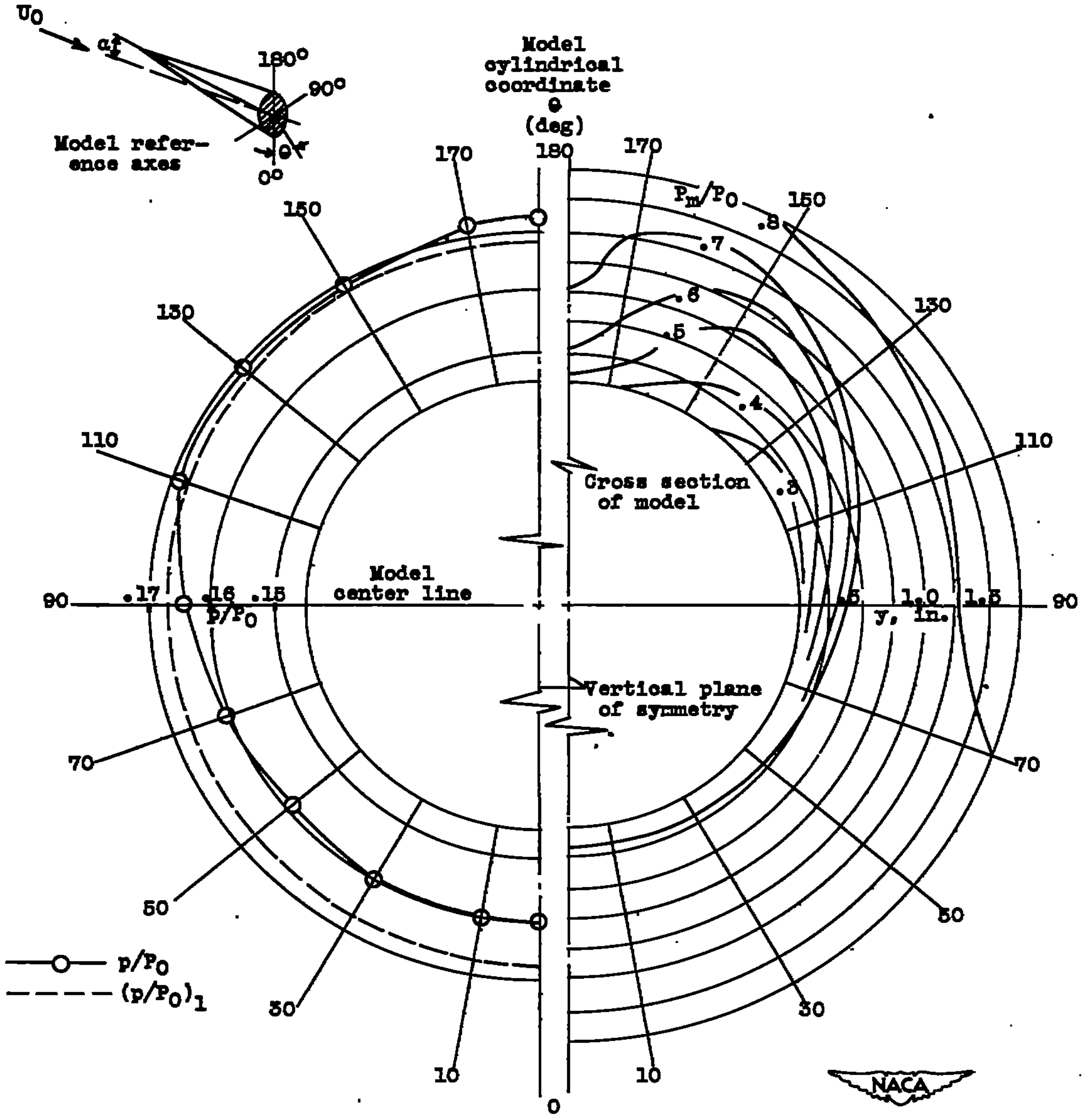

x, 70 inches; free-stream pressure ratio p_0/P_0, 0.179.

x, $73\frac{1}{4}$ inches; free-stream total-pressure ratio $P_{m,0}/P_0$, 0.821.

(c) Angle of attack α, 4°.

Figure 15. - Continued. Experimental variation of ratio of static to free-stream total pressure p/P_0 on body surface and ratio of pitot to free-stream total pressure P_m/P_0 in flow field at rear of model. Mach number M_0, 1.78.

1296

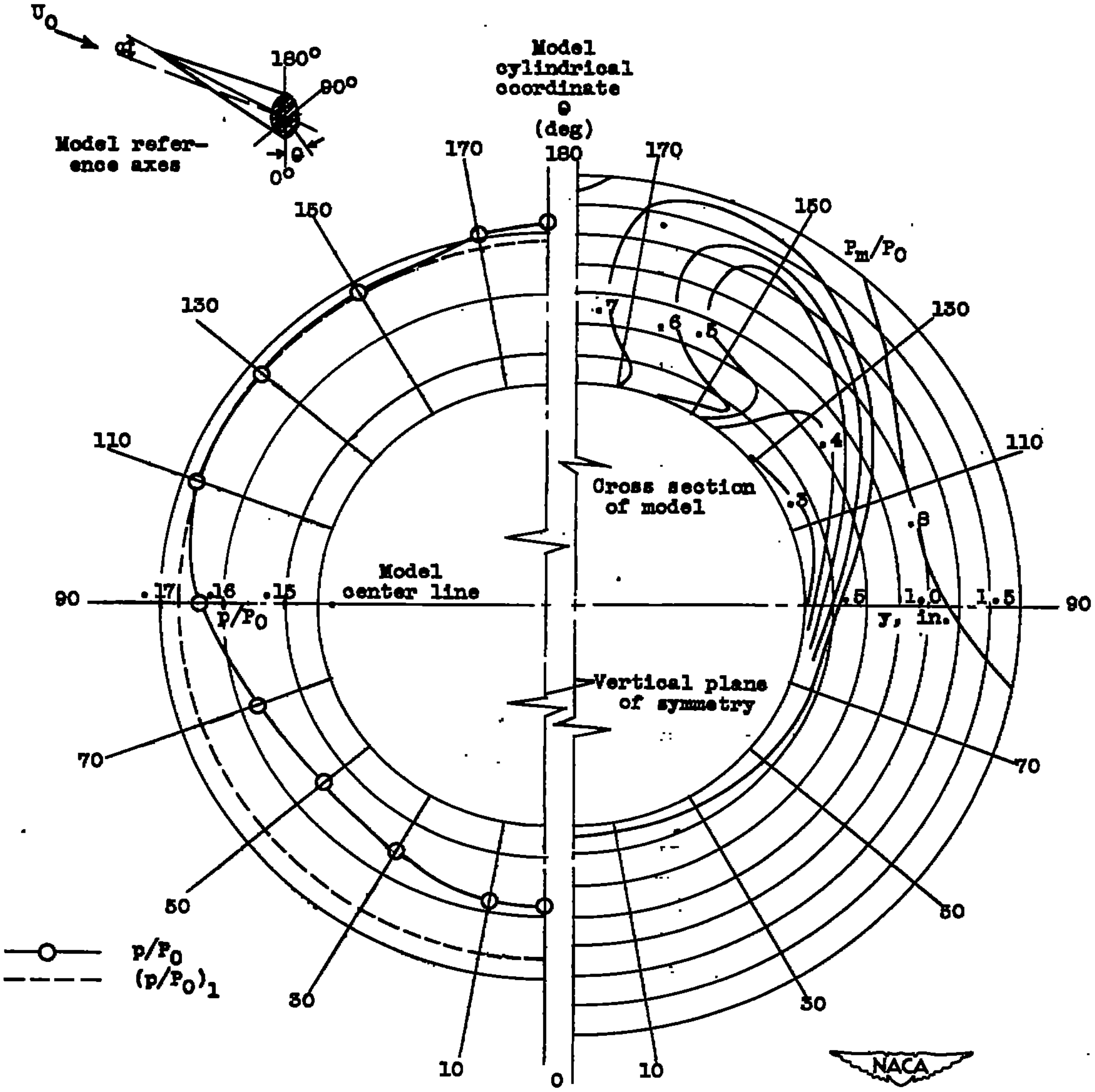

x, 70 inches; free-stream pressure ratio p_0/P_0, 0.179.

x, $73\frac{1}{4}$ inches; free-stream total-pressure ratio $P_{m,0}/P_0$, 0.821.

(d) Angle of attack α, 6°.

Figure 15. - Continued. Experimental variation of ratio of static to free-stream total pressure p/P_0 on body surface and ratio of pitot to free-stream total pressure P_m/P_0 in flow field at rear of model. Mach number M_0, 1.78.

1296

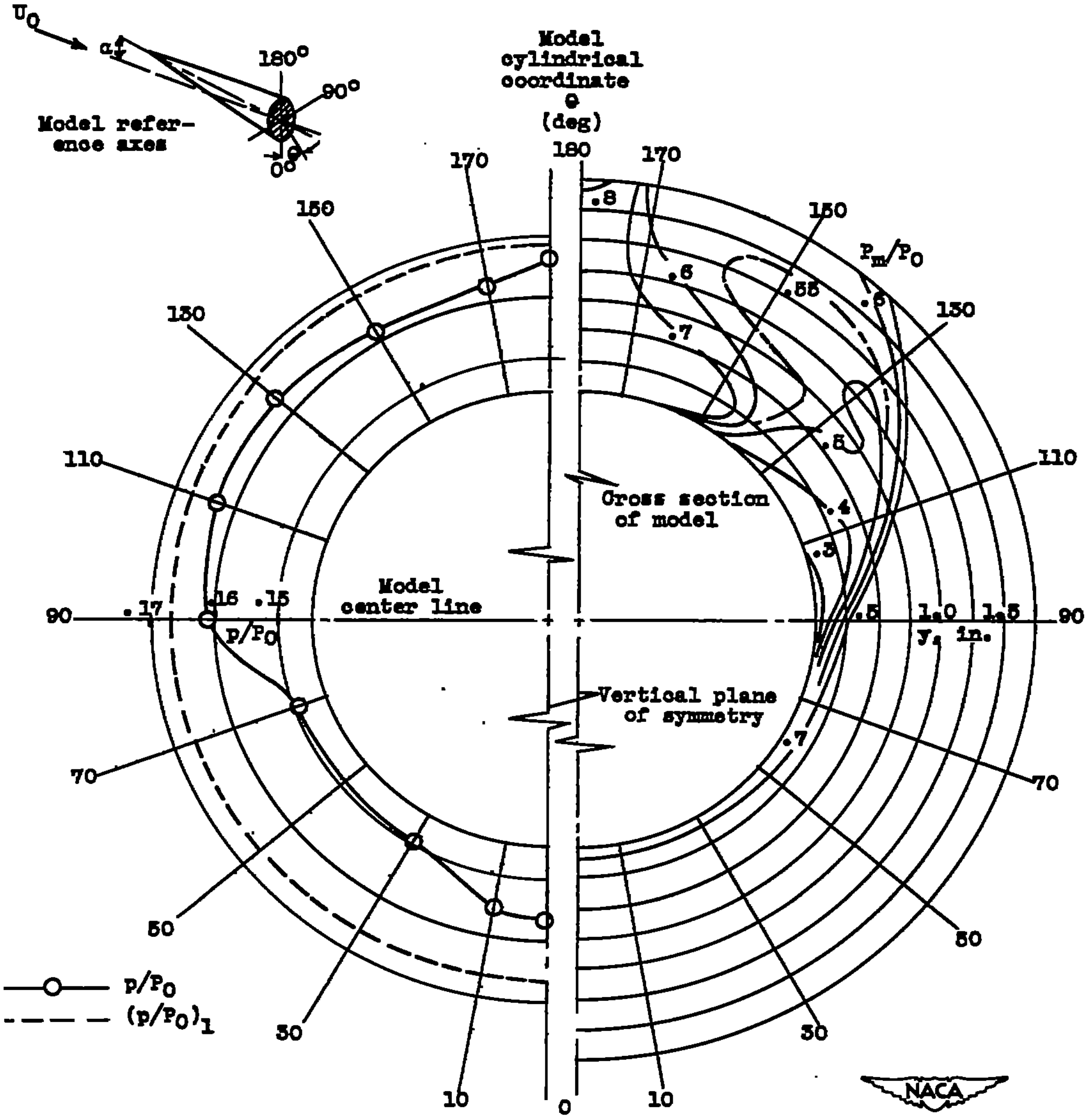

x, 70 inches; free-stream pressure ratio p_0/P_0, 0.179.

x, $73\frac{1}{4}$ inches; free-stream total-pressure ratio $P_{m,0}/P_0$, 0.821.

(e) Angle of attack α, 9°.

Figure 15. - Concluded. Experimental variation of ratio of static to free-stream total pressure p/P_0 on body surface and ratio of pitot to free-stream total pressure P_m/P_0 in flow field at rear of model. Mach number M_0, 1.78.

1296

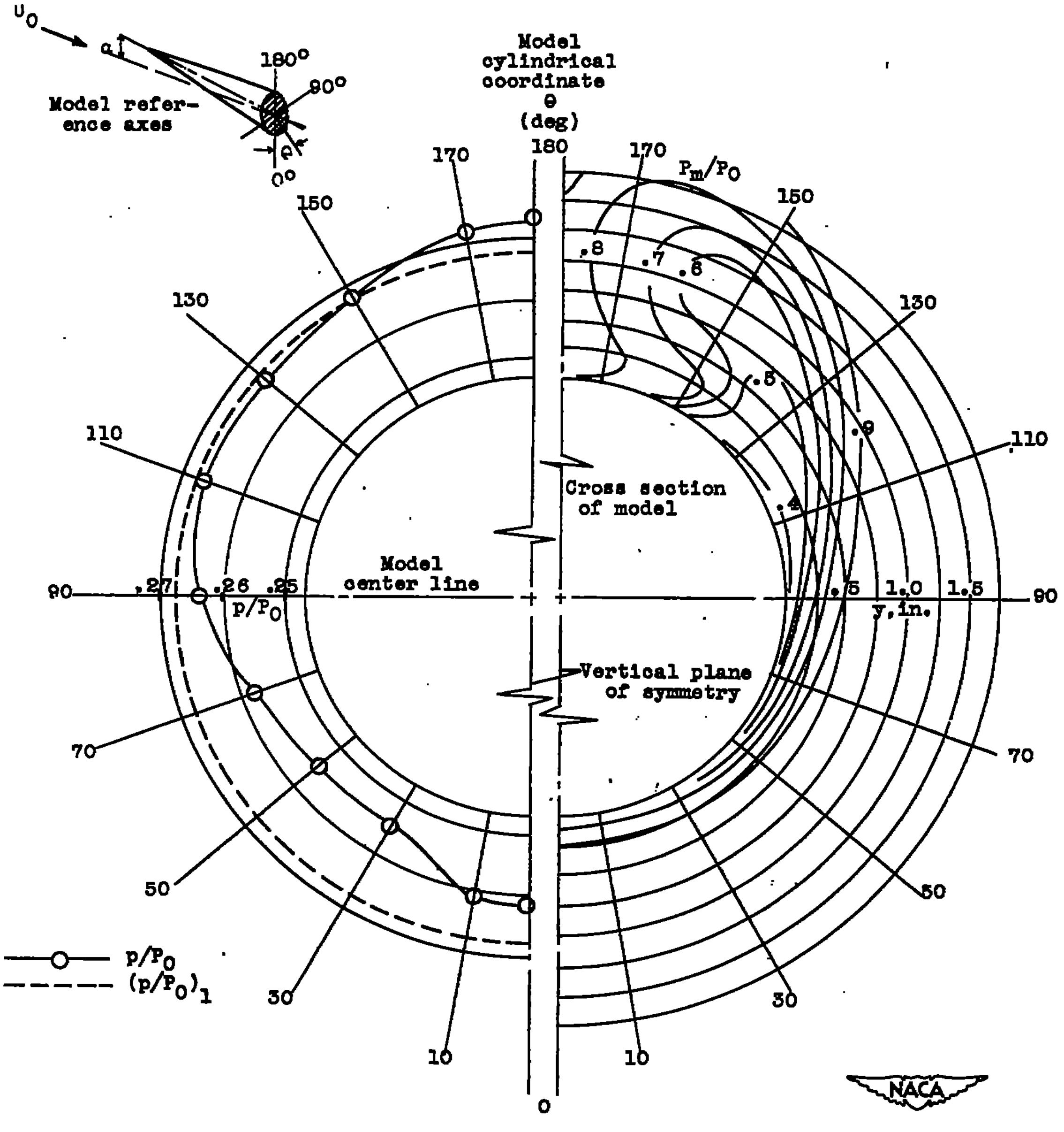

x, 70 inches; free-stream pressure ratio p_0/P_0, 0.276.

x, $73\frac{1}{4}$ inches; free-stream total-pressure ratio $P_{m,0}/P_0$, 0.933.

(a) Mach number M_0, 1.49.

Figure 16. - Experimental variation of ratio of static to free-stream total pressure p/P_0 on body surface and ratio of pitot to free-stream total pressure P_m/P_0 in flow field at rear of model. Angle of attack α, 6°.

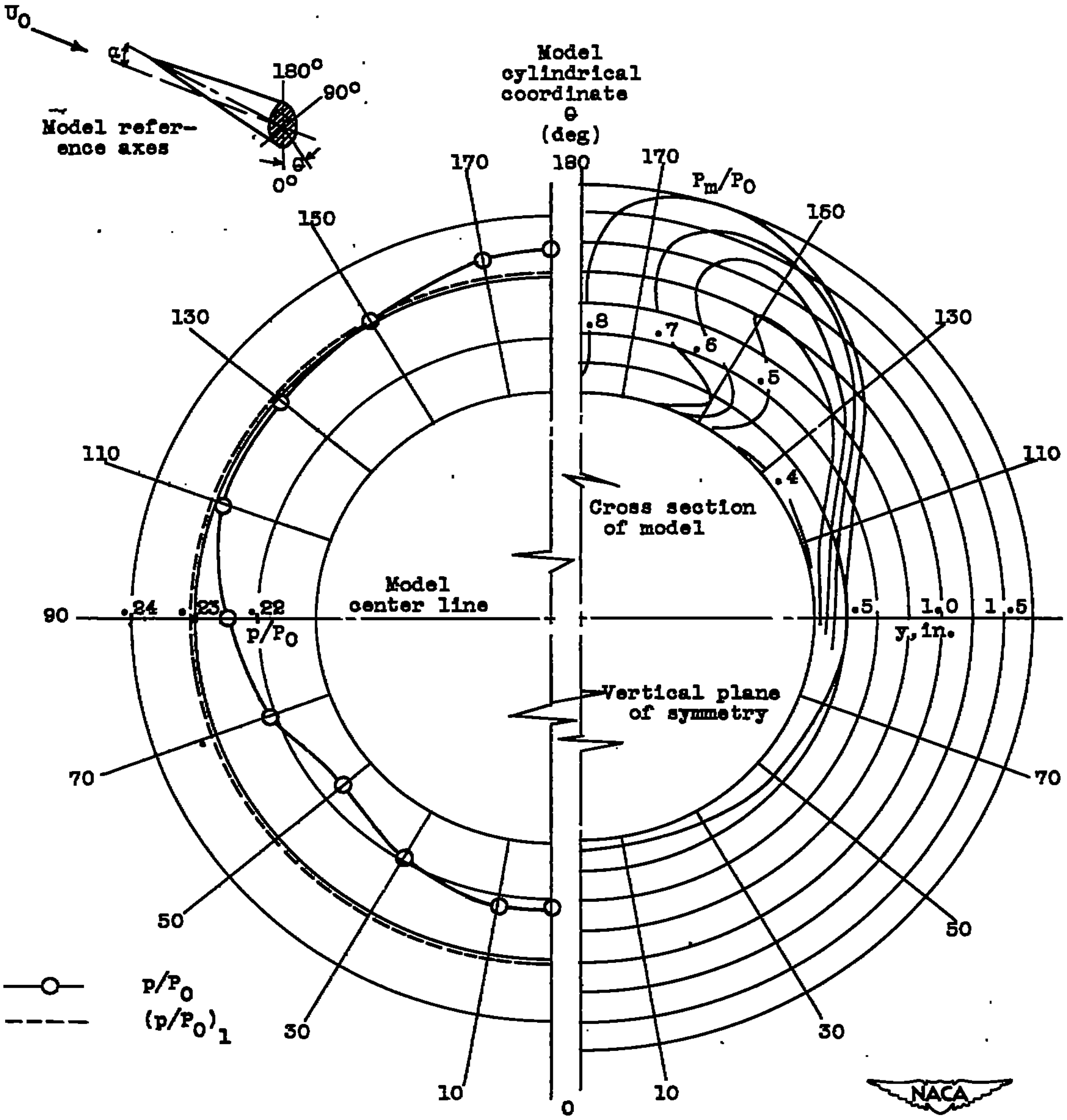

x, 70 inches; free-stream pressure ratio p_0/P_0, 0.239.

x, $73\frac{1}{4}$ inches; free-stream total-pressure ratio $P_{m,0}/P_0$, 0.903.

(b) Mach number M_0, 1.59.

Figure 16. - Continued. Experimental variation of ratio of static to free-stream total pressure p/P_0 on body surface and ratio of pitot to free-stream total pressure P_m/P_0 in flow field at rear of model. Angle of attack α, 6°.

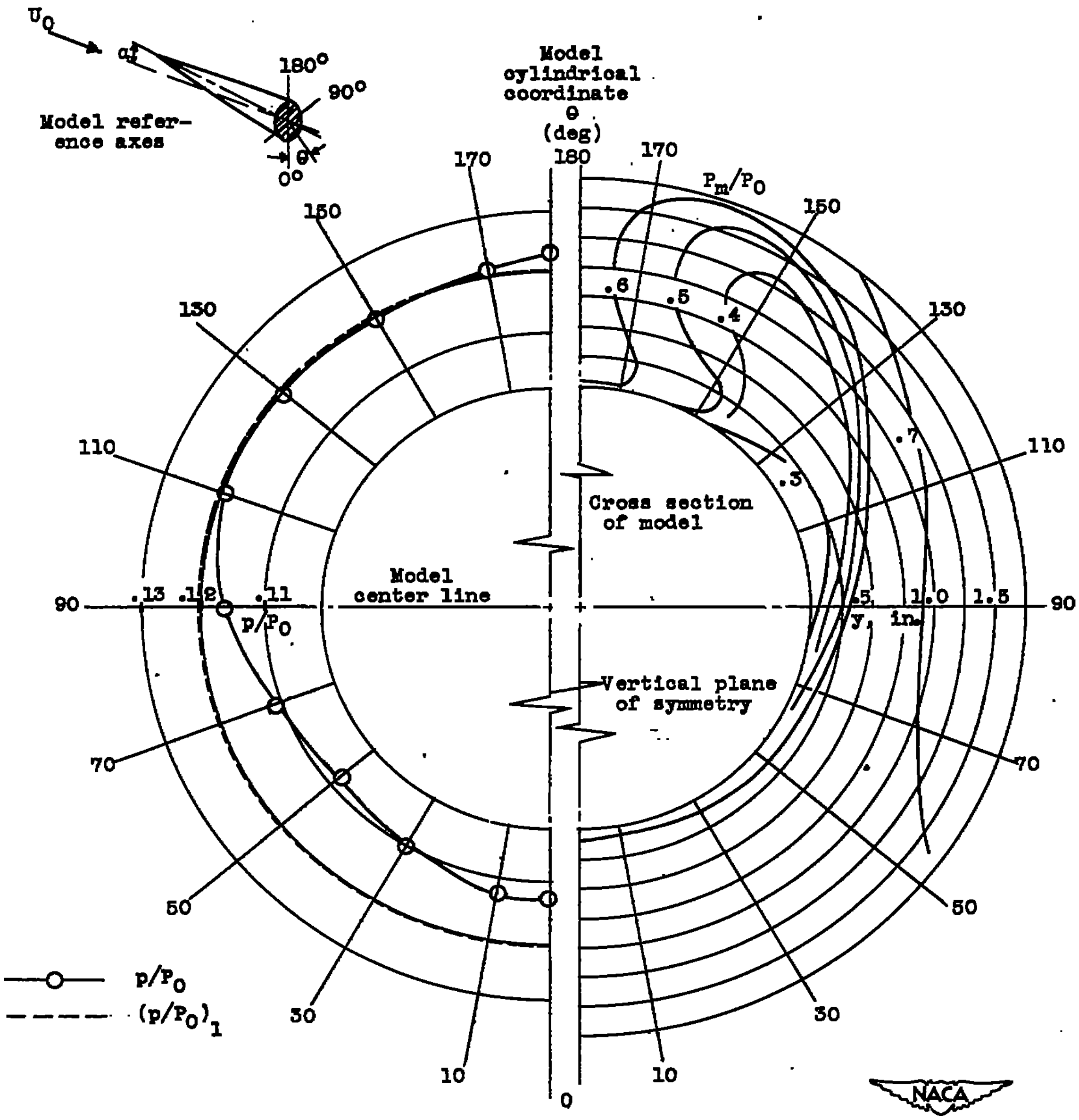

x, 70 inches; free-stream pressure ratio p_0/P_0, 0.132.

x, $73\frac{1}{4}$ inches; free-stream total-pressure ratio $P_{m,0}/P_0$, 0.730.

(c) Mach number M_0, 1.98.

Figure 16. - Concluded. Experimental variation of ratio of static to free-stream total pressure p/P_0 on body surface and ratio of pitot to free-stream total pressure P_m/P_0 in flow field at rear of model. Angle of attack α, 6°.

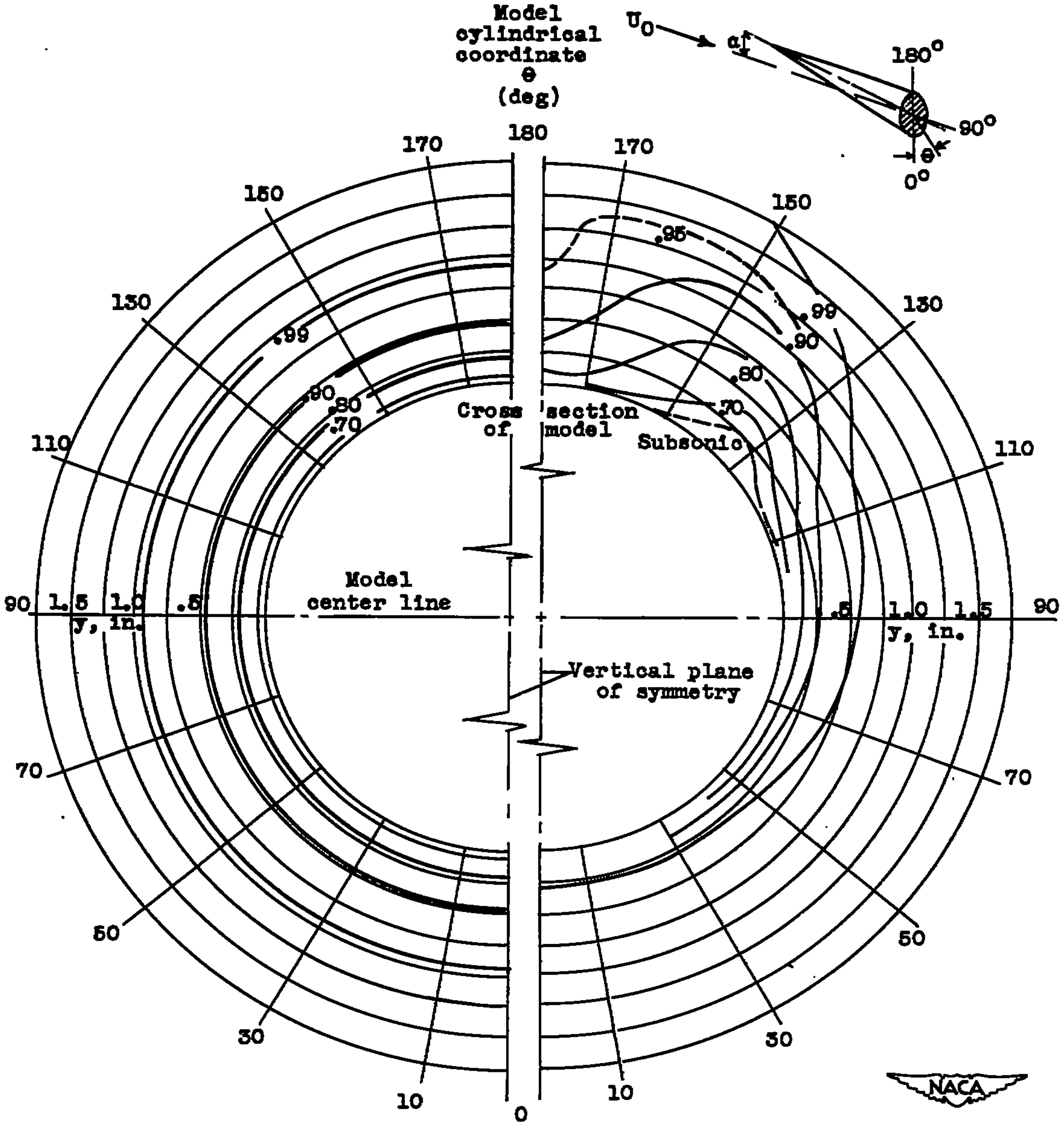

Angle of attack α, 0°. Angle of attack α, 4°.

Figure 17. - Experimental variation of contours of nondimensional boundary-layer velocity u/U_L in flow field at station $73\frac{1}{4}$ for angles of attack of 0° and 4°. Mach number M_0, 1.78.

[redacted]

[redacted]

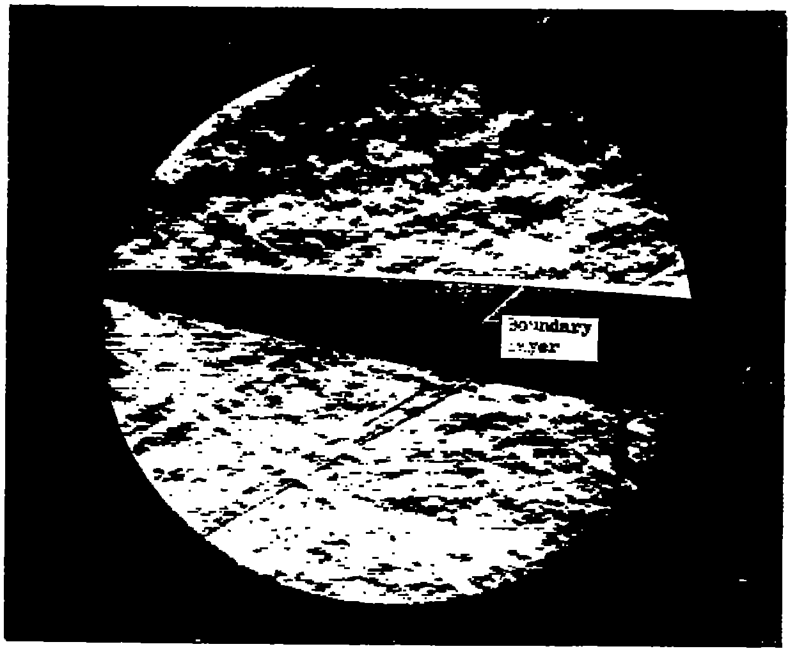

(a) Knife-edge horizontal up.

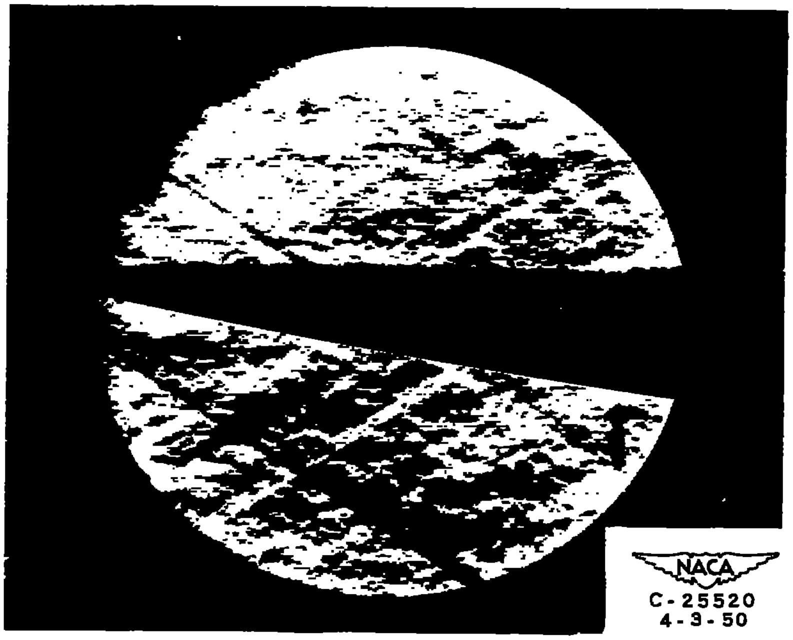

(b) Knife-edge horizontal down.

Figure 18. - Schlieren photograph of forward portion of RM-10 fuselage showing boundary-layer growth. Mach number M_0, 1.78; angle of attack α, 6°; Reynolds number Re, 31,000,000.

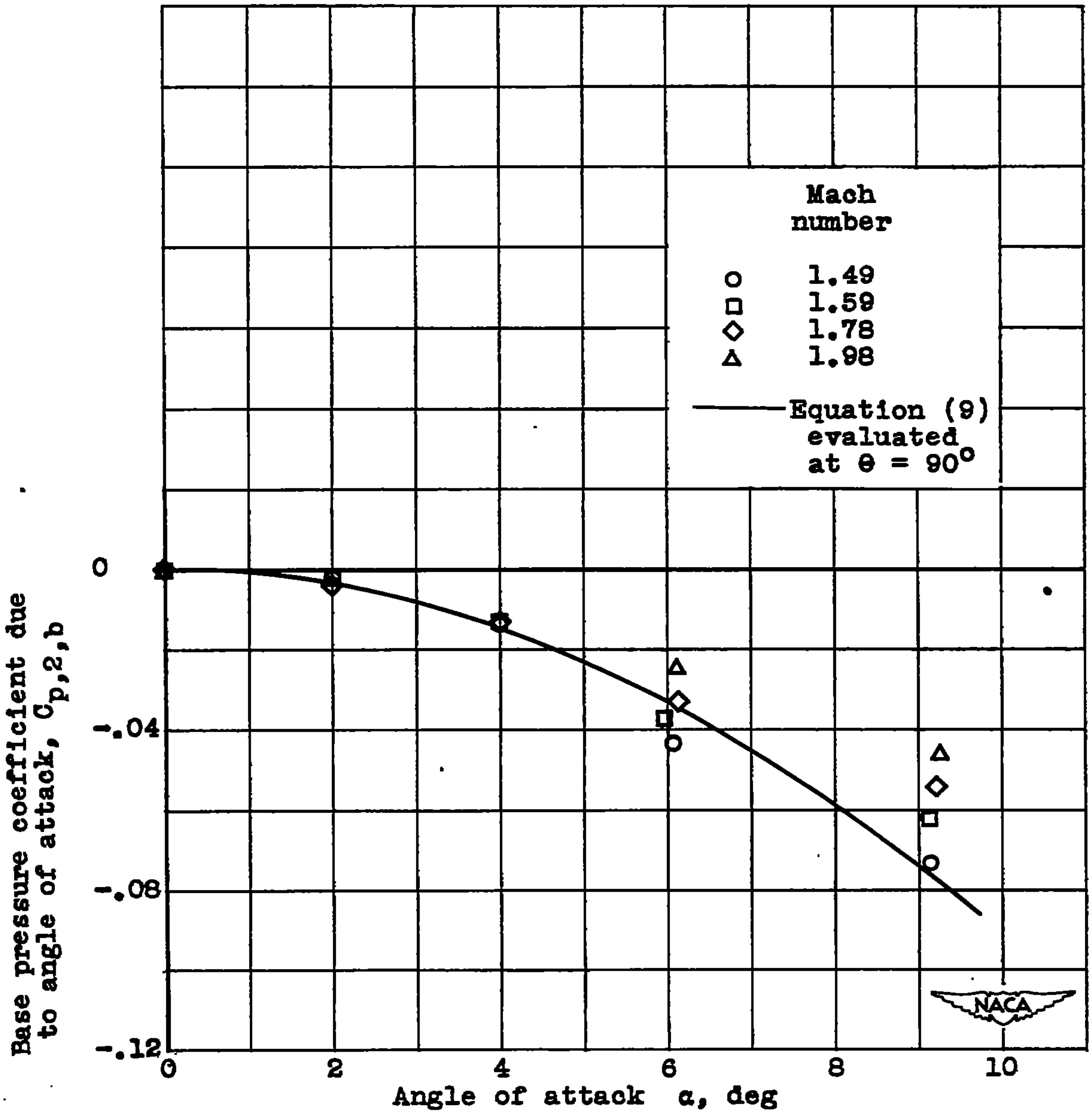

Figure 19. - Experimental variation of base pressure coefficient due to angle of attack with angle of attack for Mach numbers investigated.